The Astrophysical Journal, 791:22 (16pp), 2014 August 10 doi:10.1088/0004-637X/791/1/22

LONG-TERM VARIATION OF THE SOLAR DIURNAL ANISOTROPY OF GALACTIC COSMIC RAYS OBSERVED WITH THE NAGOYA MULTI-DIRECTIONAL MUON DETECTOR

K. Munakata[1], M. Kozai[1], C. Kato[1], and J. Kóta[2]
[1] Physics Department, Shinshu University, Matsumoto, Nagano 390-8621, Japan; kmuna00@shinshu-u.ac.jp
[2] Lunar and Planetary Laboratory, University of Arizona, Tucson, AZ 87721, USA
Received 2014 April 3; accepted 2014 June 17; published 2014 July 22

ABSTRACT

We analyze the three-dimensional anisotropy of the galactic cosmic ray (GCR) intensities observed independently with a muon detector at Nagoya in Japan and neutron monitors over four solar activity cycles. We clearly see the phase of the free-space diurnal anisotropy shifting toward earlier hours around solar activity minima in $A > 0$ epochs, due to the reduced anisotropy component parallel to the mean magnetic field. This component is consistent with a rigidity-independent spectrum, while the perpendicular anisotropy component increases with GCR rigidity. We suggest that this harder spectrum of the perpendicular component is due to contribution from the drift streaming. We find that the bi-directional latitudinal density gradient is positive in the $A > 0$ epoch, while it is negative in the $A < 0$ epoch, in agreement with the drift model prediction. The radial density gradient of GCRs, on the other hand, varies with a ∼11 yr cycle with maxima (minima) in solar maximum (minimum) periods, but we find no significant difference between the radial gradients in the $A > 0$ and $A < 0$ epochs. The corresponding parallel mean free path is larger in $A < 0$ than in $A > 0$. We also find, however, that the parallel mean free path (radial gradient) appears to persistently increase (decrease) in the last three cycles of weakening solar activity. We suggest that simple differences between these parameters in $A > 0$ and $A < 0$ epochs are seriously biased by these long-term trends.

Key words: cosmic rays – methods: data analysis – Sun: heliosphere – Sun: magnetic fields

1. INTRODUCTION

The solar wind is a supersonic plasma blowing radially outward from the Sun toward a vast space filled by cold and thin interstellar plasma. The global structure of the region called the "heliosphere," which is a region dominated by solar wind plasma and the solar magnetic field, is of great interest for both solar- and astrophysicists. The interplanetary magnetic field (IMF) is the term representing the solar magnetic field carried outward by solar wind into the heliosphere as magnetic field lines from the Sun are dragged along by the highly conductive solar wind plasma (Parker 1958). Because of the dominant dipole component of the solar magnetic field, the IMF is divided into two magnetic sectors in the northern and southern hemisphere separated by the heliospheric current sheet (HCS), which develops into a "wavy" three-dimensional (3D) structure. The inclination of the magnetic dipole from the rotation axis increases with increasing solar activity and reverses during the solar activity maximum epoch when the inclination reaches its maximum. The Sun has a strong and complex magnetic field, and the physical properties of the heliosphere are directly connected to the properties of the magnetic field, varying with a period of about 11 yr.

Temporal variations in the inner heliosphere can be deduced from the ground-based observations of the high-energy galactic cosmic rays (GCRs). GCRs are high-energy nuclei (mostly protons) accelerated in our Galaxy and continuously arriving at the Earth after traveling through the heliosphere. After entering the heliosphere, GCRs interact with the IMF being carried outward by solar wind. The interaction with the large-scale ordered field causes the gradient- and curvature-drift motions of GCRs in the heliosphere, while the interaction with the irregular (or disordered) field component results in the pitch angle scattering of GCRs. Scattering by the magnetic irregularities embedded in the expanding solar wind causes the deceleration (called the adiabatic cooling) and also causes an outward convection, which leads to lower GCR intensities closer to the Sun. The resulting positive radial gradient of GCRs produces an inward diffusion, flowing preferentially along the ordered IMF lines. A steady-state distribution is realized when the inward diffusion is balanced with the outward convection. The GCR intensity measured at the Earth changes with various timescales. The solar cycle variation of the solar wind parameters, such as the solar wind velocity, the magnitude and orientation of the IMF, the tilt angle of the HCS, and the mean free path of the pitch angle scattering of GCRs in the turbulent magnetic field, alters the spatial distribution of GCR density in the heliosphere. The drift model of GCR transport predicts a bi-directional latitudinal gradient pointing in opposite directions on opposite sides of the HCS if the HCS is flat (Jokipii & Kopriva 1979). The predicted spatial distribution of the GCR density has a minimum along the HCS in the "positive" polarity period of the solar polar magnetic field (also referred as the $A > 0$ epoch) when the IMF directs away from (toward) the Sun in the northern (southern) hemisphere, while the distribution has a local maximum on the HCS in the "negative" period ($A < 0$ epoch) with opposite field orientation in each hemisphere. The field orientation reverses every 11 yr around the maximum period of solar activity. A tilted current sheet introduces modifications around the wavy HCS. For example, the intensity minimum (for $A > 0$) will not be right at the HCS, but the general tendencies in the sense of the latitudinal gradient remain the same as outlined above (Jokipii & Kóta 1982).

The variation of the spatial distribution of GCR density causes the variation in the directional anisotropy of the GCR intensity measured at the Earth. One such variation is the 22 yr variation of the solar diurnal anisotropy in which the phase (or the local solar time of maximum intensity) of the anisotropy shifts toward earlier hours around every $A > 0$ solar minimum (Thambyahpillai & Elliot 1953; Forbush 1967; Ahluwalia

1988; Bieber & Chen 1991, and references therein). By analyzing the anisotropy observed with neutron monitors (NMs) in 1968–1988, Chen & Bieber (1993, hereafter referred as Paper I) revealed that the observed phase shift of the diurnal anisotropy is due to the decrease in the diffusion streaming parallel to the IMF in $A > 0$ solar minima. The parallel diffusion streaming is proportional to the radial gradient (G_r) of the GCR density multiplied by the parallel mean free path ($\lambda_\parallel$) of the pitch angle scattering. The simple drift model predicts smaller G_r in the $A > 0$ epoch than in the $A < 0$ epoch if the diffusion coefficients are same in both epochs (Kóta & Jokipii 1983). Finding a significant 11 yr solar cycle variation but no clear 22 yr variation in the observed G_r, however, Paper I suggested that the smaller parallel streaming in the $A > 0$ solar minimum period was caused by the smaller $\lambda_\parallel$, possibly due to the magnetic helicity effect in the turbulent magnetic field (Paper I; Bieber & Pomerantz 1986; Bieber et al. 1987).

The GCR anisotropy (or the streaming) vector in three dimensions consists of three components, two lying in the ecliptic plane and the other pointing normal to the ecliptic plane. The two ecliptic components parallel and perpendicular to the IMF are derived from the amplitude and phase of the solar diurnal anisotropy corrected for the contribution from the radial solar wind convection. Paper I analyzed the diurnal anisotropy in free space, corrected for the geomagnetic deflection of GCR orbits, by assuming a power law type ($\propto p^\gamma$) dependence of the anisotropy amplitude on the GCR rigidity (p), with the spectral index (γ) and the upper limiting rigidity (P_u) fixed at 0 and 100 GV, respectively. The zero spectral index of the diurnal anisotropy has been assumed in many analyses based on the original convection–diffusion picture of the GCR transport in which the stationary GCR distribution in the heliosphere results from inward diffusion balancing with outward convection by the solar wind, which is independent of the rigidity (Parker 1965; Gleeson & Axford 1967; Gleeson 1969). The upper limiting rigidity (P_u) set at 100 GV was also a reasonable assumption for the analysis of NM data alone, because P_u representing the break-down rigidity of the diffusion picture is expected to be much higher than the median primary rigidity to which the NMs used in Paper I respond. Munakata et al. (1997) assumed $\gamma = 0$, but treated P_u as a free parameter in their analyses of the diurnal anisotropy observed with multi-directional muon detectors (MDs), which have median responses to GCRs with higher rigidity than NMs. They found P_u changing between 100 and 300 GV in a clear correlation with the solar activity (Munakata et al. 2002). Hall et al. (1997) treated both γ and P_u as free parameters in their analyses of the NM and MD data and reported the temporal variation of each parameter in solar activity and solar magnetic cycles.

All of these works take into account the rigidity dependence of the amplitude varying as a function of time, but they still assume that the phase is independent of rigidity. In other words, they assumed a common rigidity spectrum for two ecliptic components parallel and perpendicular to the IMF. Bieber & Chen (1991, hereafter referred as Paper II), on the other hand, also reported that the magnitude of the observed phase variation in the $A > 0$ solar minimum increases with GCR rigidity (Agrawal 1983). This rigidity-dependent feature of the observed phase variation cannot be reproduced properly as long as a rigidity spectrum common to two ecliptic components is assumed. This observed feature has been confirmed by other papers (e.g., Oh et al. 2010), but its physical origin is still unknown.

The third component of the anisotropy, that is, the north–south (NS) anisotropy normal to the ecliptic plane, has been derived also from NM and MD data in a couple of different ways. Bieber & Pomerantz (1986) and Paper I derived this anisotropy from the difference between count rates in a pair of NMs located near the north and south geomagnetic poles and observing intensities of GCRs arriving from the north and south pole orientations, respectively. They found a ~10 yr cycle variation in this component anisotropy, which implies that the radial gradient (G_r) of the GCR density changes with the solar activity, but they found no significant difference in G_r in the $A > 0$ and $A < 0$ epochs, contradicting the simple drift model prediction. Due to a 23.°4 inclination of Earth's rotation axis from the ecliptic normal, the NS anisotropy normal to the ecliptic plane can be also observed as a diurnal variation of the count rate in the sidereal time with the maximum phase at ~06:00 or ~18:00 local sidereal time (Swinson 1969; Hall et al. 1996). Yasue (1980) analyzed this sidereal diurnal variation observed by NMs and MDs during 5 yr between 1969 and 1973 and found that observations were reproduced best by the average rigidity spectrum with $\gamma = 0.3$ and $P_u = 200$ GV. This was the first experimental indication that the rigidity spectrum of the anisotropy has a positive spectral index. Hall et al. (1994) also applied the same method to NM and MD data observed between 1957 and 1985 and found an average spectrum with $\gamma = 0.5$ and $P_u = 400$ GV, again with a positive γ. This suggested that both of the ecliptic components may also have a spectrum with non-zero γ.

A possible drawback of deriving the NS anisotropy from the sidereal diurnal variation is that the expected amplitude of the sidereal diurnal variation (~0.03%) is approximately an order of magnitude smaller than the solar diurnal variation (~0.3%). The small signal in the sidereal time can be easily influenced by the solar diurnal anisotropy change over a year. Another difficulty is that one can obtain only the yearly mean anisotropy. This is because of the fact that the influence from the solar diurnal variation, even if it is stationary through a year, can be eliminated in the sidereal time only when the diurnal variation is averaged over an integral year(s). This makes it difficult to deduce reliable errors of the yearly mean anisotropy. Mori & Nagashima (1979) proposed another way to derive the NS anisotropy from the "GG component" of a multi-directional MD at Nagoya in Japan. The GG component is a difference combination between intensities recorded in the north- and south-viewing directional channels designed to measure the NS anisotropy free from the atmospheric temperature effect (Nagashima et al. 1972). Laurenza et al. (2003) showed that the GG component can be used to derive reliable sector polarity of the IMF. Using a global network of four multi-directional MDs that are capable of observing the NS anisotropy on an hourly basis, Okazaki et al. (2008) confirmed that the NS anisotropy deduced from the GG component is consistent with the anisotropy observed with the global network.

In this paper, we extend the analysis of Paper I to the most recent period and derive the long-term variation of the modulation parameters from the 3D anisotropy observed over 44 yr by the Nagoya multi-directional MD, which has a median rigidity of 60 GV for primary GCRs. We also analyze the anisotropy observed during the same period by NMs that have a median response to 17 GV primary GCRs. We derive the NS anisotropy from the GG component of the Nagoya MD. We particularly examine the rigidity dependences of each component of the anisotropy and each modulation parameter by

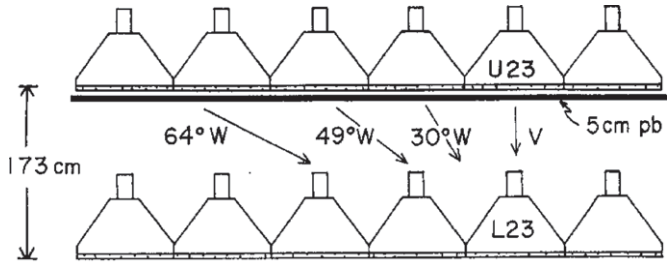

Figure 1. Nagoya multi-directional muon detector. This figure is supplied from a document available at the Web site (see the text). The Nagoya muon detector (MD) consists of two horizontal 6 × 6 arrays of 1 m^2 unit detectors, vertically separated by 1.73 m, with an intermediate 5 cm layer of lead to absorb the soft component radiation in the air. Each unit detector has a 1 m × 1 m plastic scintillator viewed by a photomultiplier tube of 12.7 cm diameter. By counting the pulses of the twofold coincidences between a pair of detectors on the upper and lower layers, the Nagoya MD records the rate of muons from the corresponding incident direction, as shown in this figure. The multi-directional MD comprises various combinations between the upper and lower detectors. The directional channels named "30°W," "49°W," and "64°W" in this figure correspond to "W," "W2," and "W3" in Table 1, respectively. The geomagnetic cutoff rigidity (P_c) and median primary rigidity (P_m) in GV are listed in Table 1.

comparing them as derived from MD and NM data at 60 GV and 17 GV, respectively. We do not intend to determine each rigidity spectrum quantitatively by, for instance, calculating both γ and P_u as free parameters in the best-fit calculation as a function of time. In such best-fit calculations, we often see a significant anti-correlation between the best-fit γ and P_u (Hall et al. 1994, 1997). A large P_u with a small (or negative) γ often returns a χ^2 value similar to that of a small P_u with a large (or positive) γ, increasing the systematic error of each best-fit value. We instead examine the rigidity spectrum qualitatively based on the ratio between parameters derived from NM and MD data with a common assumption of the spectrum with fixed values of $\gamma = 0$ and $P_u = 100$ GV, respectively, as in Paper I. If the ratio is close to 1, the spectrum is consistent with the assumption. If the ratio is significantly larger (smaller) than 1, on the other hand, we can conclude that the spectrum is harder (softer) than assumed. In this way, we can make a qualitative but reliable examination of the rigidity dependence of each parameter. We will present quantitative analyses of the rigidity dependence elsewhere. We will show in this paper that three components of the anisotropy have different rigidity dependences. This naturally explains the rigidity-dependent feature of the observed phase variation mentioned above. We will also suggest that the different rigidity dependences of the three anisotropy components are possibly due to the relative contribution from the drift (diamagnetic drift), which is different in each component.

The outline of this paper is as follows. In Section 2, we describe the data analysis and results in detail. The conclusions and discussions are given in Section 3. For references, we also present our results in a numerical data table in Appendix A. In Appendix B, we show how the obtained results depend on the assumed value of P_u.

2. DATA ANALYSES AND RESULTS

We derive the cosmic ray anisotropy in three dimensions by analyzing the pressure-corrected hourly count rates recorded by an MD at Nagoya in Japan over 44 yr between 1970 and 2013. The Nagoya MD is multi-directional and capable of simultaneously monitoring intensities in 17 directional channels of viewing (see Figure 1). It has been in operation since 1970, producing a continuous record of cosmic ray intensity over four decades and allowing us to analyze the long-term variation of the anisotropy.[3] Based on our own experience with long-term observations using plastic scintillators and PMTs similar to the Nagoya MD, we estimate that the absolute muon count rate by the Nagoya MD has decreased ∼10% or less in four decades due to the deterioration of detectors. The effect of this deterioration, however, should be negligibly small for the GCR anisotropy analyzed in this paper, because our analysis does not use the absolute count rate but the fractional deviation of the count rate from the daily or monthly mean, as shown later in this section. The median rigidity (P_m) of primary GCRs, calculated utilizing the response function of the atmospheric muons to the primary particles (Murakami et al. 1979), ranges from 59.4 to 113.7 GV, and the statistical error of the hourly count rate ranges between 0.06% and 0.28% (Okazaki et al. 2008). In this paper, we use 60 GV for the representative P_m of the Nagoya MD. The response function has been first calculated for each element in the GCRs and then averaged with a weight according to the observed elemental abundance of GCRs (Murakami et al. 1979).

We also derive the anisotropy by analyzing the data recorded during the same period by NMs, Swarthmore/Newark, Alert/Thule, and McMurdo, each of which have a P_m of 17 GV (Yasue et al. 1982). We use the data from Swarthmore/Newark to derive the diurnal anisotropy, while we derive the NS anisotropy from a pair of polar NMs at Thule in Greenland (or Alert in Canada) and McMurdo in Antarctica.[4] By comparing anisotropies derived from MDs and NMs whose P_m differ by a factor of about 3.5 from each other, we discuss the rigidity dependence of the anisotropy and its long-term variation. Table 1 summarizes the cosmic ray data analyzed in this paper.

In this section, we describe our analyses of the Nagoya MD data, while we derive the anisotropy in free space from NMs in Table 1 following the analyses in Paper I and Paper II. For our analyses of NM data, therefore, readers can refer to those papers.

2.1. Elimination of Short-term Events and Derivation of the Observed Diurnal Variation

We begin our analyses by calculating the fractional deviation $\Delta I_j(t)$ of the pressure-corrected hourly muon count rate $I_j(t)$ in the jth directional channel of the Nagoya MD ($j = 1, 2, \ldots, 17$) at the universal time t from the 24 hr central moving average $\bar{I}_j^{24h}(t)$, as

$$\Delta I_j(t) = \left(I_j(t) - \bar{I}_j^{24h}(t)\right) \Big/ \bar{I}_j^{24h}(t), \quad (1)$$

where

$$\bar{I}_j^{24h}(t) = \frac{1}{24} \sum_{t-12}^{t+11} I_j(t). \quad (2)$$

For the following analyses of the diurnal anisotropy, we use $\Delta I_j(t)$ in Equation (1) instead of $I_j(t)$ itself to avoid the influence of the gradual intensity variation, such as the day-to-day variation, on the diurnal variation. We then check the difference between the maximum and minimum values of $\Delta I_{NM}(t)$ for the McMurdo NM data in each day and exclude any days with a difference exceeding 2.0% from further analyses

[3] A description and data of the Nagoya MD are available at http://www.stelab.nagoya-u.ac.jp/ste-www1/div3/muon/muon1.html.
[4] A description and data of the NMs are available at http://neutronm.bartol.udel.edu/ and http://center.stelab.nagoya-u.ac.jp/WDCCR/.

Table 1
Neutron Monitors (NMs) and Muon Detectors (MD) Used in This Paper

DetectorType	Station (Geographic Lat., Long.)	P_c (GV)	P_m (GV)
NM[a]	Swarthmore/Newark (39.°70, −75.°70)	2.0 GV	17.0 GV
	Thule (76.°60, −68.°80)	0.0 GV	17.0 GV
	Alert (82.°50, −62.°30)	0.0 GV	17.0 GV
	McMurdo (−77.°95, 166.°60)	0.0 GV	17.0 GV
	Nagoya (35.°15, 139.°97)		
	Directional channel		
MD	V	10.1 GV	59.4 GV
	N	10.8 GV	64.6 GV
	S	10.0 GV	62.6 GV
	E	12.8 GV	66.7 GV
	W	9.7 GV	61.8 GV
	NE	12.9 GV	72.0 GV
	NW	9.1 GV	66.6 GV
	SE	11.5 GV	69.3 GV
	SW	9.5 GV	65.6 GV
	N2	8.6 GV	83.0 GV
	S2	9.5 GV	80.5 GV
	E2	13.2 GV	88.3 GV
	W2	8.7 GV	79.3 GV
	N3	8.7 GV	105.0 GV
	S3	9.5 GV	103.7 GV
	E3	17.1 GV	113.7 GV
	W3	8.6 GV	103.0 GV

Notes. The geomagnetic cut-off rigidity (P_c) and median primary rigidity (P_m) in GV are listed for each directional channel together with the geographic latitude and longitude of the location of the detector in degrees. The Nagoya MD has 17 directional channels, while each NM measures only omni-directional intensity which is regarded as the vertical intensity on average.

[a] For deriving the diurnal anisotropy at 17 GV, we use Swarthmore NM data for a period between 1970 and 1978, while we use Newark NM data for a period between 1979 and 2013. For deriving the north–south anisotropy at 17 GV, we use Thule and McMurdo NMs for two periods, one between 1970 and 1975 and the other between 1979 and 2013, while we use Alert and McMurdo for a period between 1976 and 1978.

to avoid the influence of large cosmic ray events such as the Forbush decreases. A total of 777 days are excluded out of 16,071 days in 44 yr between 1970 and 2013 in our analyses of MD and NM data. We confirmed that these excluded days include the majority of cosmic ray events reported so far (Cane et al. 1996; Jordan et al. 2011). From $\Delta I_j(t)$ in the remaining days, we obtain the monthly mean diurnal distribution, $d_j(t_k)$, of $\Delta I_j(t)$ as a function of the local solar time $t_k (k = 1, 2, \ldots, 24)$ at the observation site, Nagoya, in Japan.

We then deduce the diurnal variation of GCR intensity from the Fourier analysis of $d_j(t_k)$ described above, as

$$a_{1,j}^{1,\mathrm{obs}} = \frac{1}{\pi}\sum_{k=1}^{24} d_j(t_k)\cos(\omega t_k) \tag{3a}$$

$$b_{1,j}^{1,\mathrm{obs}} = \frac{1}{\pi}\sum_{k=1}^{24} d_j(t_k)\sin(\omega t_k), \tag{3b}$$

where $a_{1,j}^{1,\mathrm{obs}}$ and $b_{1,j}^{1,\mathrm{obs}}$ are the observed harmonic components of the monthly average diurnal variation and ω is $\pi/12$. In the following subsections, we use $a_{1,j}^{1,\mathrm{obs}}$ and $b_{1,j}^{1,\mathrm{obs}}$ to derive the diurnal anisotropy at 60 GV in free space corrected for the geomagnetic effects by accounting for the energy response of each directional channel. We use $a_{1,j}^{1,\mathrm{obs}}$ and $b_{1,j}^{1,\mathrm{obs}}$ observed by the Newark/Swarthmore NM during the same period to derive the free space diurnal anisotropy at 17 GeV (see Paper II).

2.2. Correction for the Compton–Getting Effect Arising from the Earth's Orbital Motion Around the Sun

The Earth's orbital motion around the Sun causes an apparent anisotropy due to the Compton–Getting (CG) effect (Compton & Getting 1935; Cutler & Groom 1986; Amenomori et al. 2004). The amplitude and phase of this apparent anisotropy in space are known to be independent of the particle's rigidity p. Space harmonic components of this anisotropy, ξ_x^{CG} and ξ_y^{CG} in the Geocentric Solar Ecliptic Coordinate System (GSE), are given as

$$\xi_x^{\mathrm{CG}} = 0, \tag{4a}$$

$$\xi_y^{\mathrm{CG}} = -(2+\Gamma)v_E/c, \tag{4b}$$

where Γ is the power law index of the energy spectrum of GCRs, v_E is the Earth's velocity, and c is the speed of light. We set Γ and v_E to be 2.7 and 30 km s^{-1}, respectively. Note that we define the anisotropy vector throughout this paper as a vector pointing toward the direction *from* which the highest GCR flux is measured; i.e., the anisotropy vector is directed opposite to the GCR streaming vector.

The harmonic components of the diurnal variation expected from this effect for the jth directional channel of the MD are then given as

$$a_{1,j}^{1,\mathrm{CG}} = c_{1,j}^{1,\mathrm{CG}}\xi_x^{\mathrm{CG(GEO)}} + s_{1,j}^{1,\mathrm{CG}}\xi_y^{\mathrm{CG(GEO)}} \tag{5a}$$

$$b_{1,j}^{1,\mathrm{CG}} = -s_{1,j}^{1,\mathrm{CG}}\xi_x^{\mathrm{CG(GEO)}} + c_{1,j}^{1,\mathrm{CG}}\xi_y^{\mathrm{CG(GEO)}}, \tag{5b}$$

where $\xi_x^{\mathrm{CG(GEO)}}$ and $\xi_y^{\mathrm{CG(GEO)}}$ are the space harmonic components of the CG anisotropy transformed to the Geographic Coordinate System (GEO) and $c_{1,j}^{1,\mathrm{CG}}$ and $s_{1,j}^{1,\mathrm{CG}}$ are the so-called coupling coefficients relating the observed harmonic vector with the space harmonic vector, and are calculated (Fujimoto et al. 1984) as

$$c_{1,j}^{1,\mathrm{CG}} = \frac{1}{\bar{I}_j}\int_{p_{cj}}^{\infty}\int_{\Omega_j}\int_{S_j} Y\cdot G^{\mathrm{CG}}(p)\cdot P_1^1(\cos\theta_{\mathrm{or}}) \cdot\cos(\phi_{\mathrm{or}}-\phi_{\mathrm{st}})dSd\Omega dp \tag{6a}$$

$$s_{1,j}^{1,\mathrm{CG}} = \frac{1}{\bar{I}_j}\int_{p_{cj}}^{\infty}\int_{\Omega_j}\int_{S_j} Y\cdot G^{\mathrm{CG}}(p)\cdot P_1^1(\cos\theta_{\mathrm{or}}) \cdot\sin(\phi_{\mathrm{or}}-\phi_{\mathrm{st}})dSd\Omega dp. \tag{6b}$$

In Equations (6a) and (6b), $\bar{I}_j$ is the average count rate in the jth directional channel of the MD, Y is the response function of the atmospheric muons to primary GCRs, and p_{cj} is the cutoff rigidity below which Y is insignificant (Murakami et al. 1979). The response function Y gives the number of muons produced by primary particles of rigidity p and arriving at the jth directional channel with zenith angle θ and azimuth angle ϕ. $P_1^1(x)$ is the semi-normalized spherical function $P_n^m(x)$ with $n = m = 1$ (Chapman & Bartels 1940). S_j and Ω_j are, respectively, the total area and solid angle of the jth directional channel and dS and $d\Omega$ are those elements. ϕ_{st} is the geographic longitude of the detector site and θ_{or} and ϕ_{or} are, respectively, the geographic co-latitude and longitude defining the asymptotic direction outside

the geomagnetic field of primary particles with p, which produce muons with the incident direction (θ, ϕ), as determined using a particle trajectory code (Lin et al. 1995). The integrals in Equations (6a) and (6b) are higher than all rigidity values for which primary particles produce detectable muons and all incident directions (θ, ϕ) for which muons can enter the jth directional channel. In Equations (6a) and (6b), $G^{\rm CG}$ is the rigidity spectrum of the CG anisotropy and is independent of p, as

$$G^{\rm CG}(p) = 1. \quad (7)$$

Using Equations (5a) and (5b) as an example, we briefly describe a physical implication of the coupling coefficients. The phase of the CG anisotropy in space given in Equations (4a) and (4b) is 270° in the GSE longitude, or 06:00 hr in local solar time. With the coupling coefficients $c^{1,\rm CG}_{1,j}$ and $s^{1,\rm CG}_{1,j}$ in Equations (6a) and (6b), which are both positive for the vertical channel of the Nagoya MD, we get $a^{1,\rm CG}_{1,j}$ and $b^{1,\rm CG}_{1,j}$ in Equations (5a) and (5b), both positive for this channel, representing the phase of the observed anisotropy shifted to earlier hours from 06:00 hr in space due to the deflection of orbits of positively charged GCRs in the geomagnetic field. In case of $a^{1}_{1,j}$ and $b^{1}_{1,j}$, due to the unknown anisotropy, we can use the coupling coefficients to correct the observed anisotropy for the geomagnetic deflection by solving equations like (5a) and (5b) for the unknown anisotropy (ξ_x, ξ_y) in space.

As described below, we correct the observed diurnal variation for the CG effect by subtracting the expected harmonic components $a^{1,\rm CG}_{1,j}$ and $b^{1,\rm CG}_{1,j}$ in Equations (5a) and (5b) from the observed components $a^{1,\rm obs}_{1,j}$ and $b^{1,\rm obs}_{1,j}$ in Equations (3a) and (3b), respectively.

2.3. Derivation of the 3D Anisotropy in Free Space

The 3D anisotropy of the GCR intensity consists of three components, two lying in the ecliptic plane and the third pointing normal to the ecliptic plane. The ecliptic components are observed as the diurnal variation in solar time of the GCR intensity recorded with a ground-based detector, while the normal component is observed as the NS anisotropy. In the following subsections, we deduce the diurnal anisotropy and the NS anisotropy at 60 GV from Nagoya MD data, while we derive the anisotropy at 17 GV from NM data in Table 1.

2.3.1. Modeling Harmonic Components of the Diurnal Variation

The harmonic components $a^{1,\rm obs}_{1,j}$ and $b^{1,\rm obs}_{1,j}$ of the diurnal anisotropy observed using the Nagoya MD are expressed in terms of the unknown harmonic components $\xi^{\rm GEO}_x$ and $\xi^{\rm GEO}_y$, representing the diurnal anisotropy in free space in GEO as

$$a^{1}_{1,j} = a^{1,\rm CG}_{1,j} + c^{1}_{1,j}\xi^{\rm GEO}_x + s^{1}_{1,j}\xi^{\rm GEO}_y + a_{\rm com} \quad (8a)$$

$$b^{1}_{1,j} = b^{1,\rm CG}_{1,j} - s^{1}_{1,j}\xi^{\rm GEO}_x + c^{1}_{1,j}\xi^{\rm GEO}_y + b_{\rm com}, \quad (8b)$$

where $c^{1}_{1,j}$ and $s^{1}_{1,j}$ are the coupling coefficients given by Equations (6a) and (6b) with $G^{\rm CG}(p)$ replaced with $G(p)$ for the unknown rigidity spectrum of the diurnal anisotropy. In Equations (8a) and (8b), $a_{\rm com}$ and $b_{\rm com}$ are harmonic components of the diurnal variation arising from the atmospheric temperature effect on muon intensity, which is assumed in this paper to be common for all directional channels as the first-order approximation. For $G(p)$, we assume in this paper

$$G(p) = 1 \quad \text{for } p \leqslant P_u$$
$$= 0 \quad \text{for } p > P_u, \quad (9)$$

where P_u is the upper limiting rigidity of the anisotropy and is set to be constant at 100 GV. This spectrum is used in Paper II for the analysis of NM data, and we use the same spectrum for MD data as well. Results derived with different P_u are shown and discussed in Appendix B.

2.3.2. Deriving the Diurnal Anisotropy in Free Space

We deduce the best-fit parameters $\xi^{\rm GEO}_x$, $\xi^{\rm GEO}_y$, $a_{\rm com}$, and $b_{\rm com}$ in Equations (8a) and (8b) that minimize the residual S, defined as

$$S = \sum_{j=1}^{17} \left\{ \left(a^{1,\rm obs}_{1,j} - a^{1}_{1,j}\right)^2 / \sigma^2_{a,j} + \left(b^{1,\rm obs}_{1,j} - b^{1}_{1,j}\right)^2 / \sigma^2_{b,j} \right\}, \quad (10)$$

where $\sigma_{a,j}$ and $\sigma_{b,j}$ are errors of $a^{1,\rm obs}_{1,j}$ and $b^{1,\rm obs}_{1,j}$, respectively, and are deduced from the dispersion of $\Delta I_j(t)$ used for calculating the monthly mean $d_j(t_k)$ at the local time t_k in Equations (3a) and (3b). We perform this calculation for every month and calculate yearly mean values and errors of $\xi^{\rm GEO}_x$, $\xi^{\rm GEO}_y$, $a_{\rm com}$, and $b_{\rm com}$ from means and dispersions of 12 monthly values, respectively. Figure 2 displays sample comparisons between the best-fit and the observed yearly mean harmonic vectors for the Nagoya MD in 2002 and 1976 when the solar activity was close to the maximum and minimum, respectively. It is clear that the amplitude of the derived space harmonic vector indicated in each panel is significantly larger in 2002 than that in 1976, causing an "expansion" of the pattern drawn by lines connecting the heads of harmonic vectors observed by 17 directional channels during the solar maximum period. It is also clear that the phase of the derived space harmonic vector is about 4 hr earlier in 1976 than in 2002, due to the 22 yr variation of the diurnal anisotropy.

2.3.3. Identification of IMF Sector and Solar Dipole Magnetic Field Polarities

In order to calculate the diurnal anisotropy in each IMF sector, we identify the sector polarity (*toward* or *away*) of each day, referring to the polarity of the Stanford Mean Magnetic Field of the Sun (see the WSO Web site at http://wso.stanford.edu/) with the date shifted 5 days later for a rough correction of the solar wind transit time between the Sun and the Earth. For the period prior to 1975 when the data are not available on the WSO Web site, we identify the polarity using the IMF data in the National Space Science Data Center's "omnitape" (King & Papitashvili 2005) following the analysis in Paper II. Because of serious gaps in the "omnitape" data, particularly in 1980s and 1990s, we do not use the "omnitape" IMF data for an entire period in this analysis. By analyzing a period when both the Stanford Mean Magnetic Field and the "omnitape" data are available, we confirmed that the daily sector polarities identified by these two methods are quite consistent with each other, giving essentially the same results from our cosmic ray data analyses.

We then calculate the average diurnal distribution, $d^T_j(t_k)$ ($d^A_j(t_k)$), for *toward* (*away*) days in each month. Using $d^T_j(t_k)$ ($d^A_j(t_k)$) for $d_j(t_k)$ in Equations (3a) and (3b) and for the best-fit calculation described above, we obtain $\xi^{\rm GEO(T)}_x$, $\xi^{\rm GEO(T)}_y$,

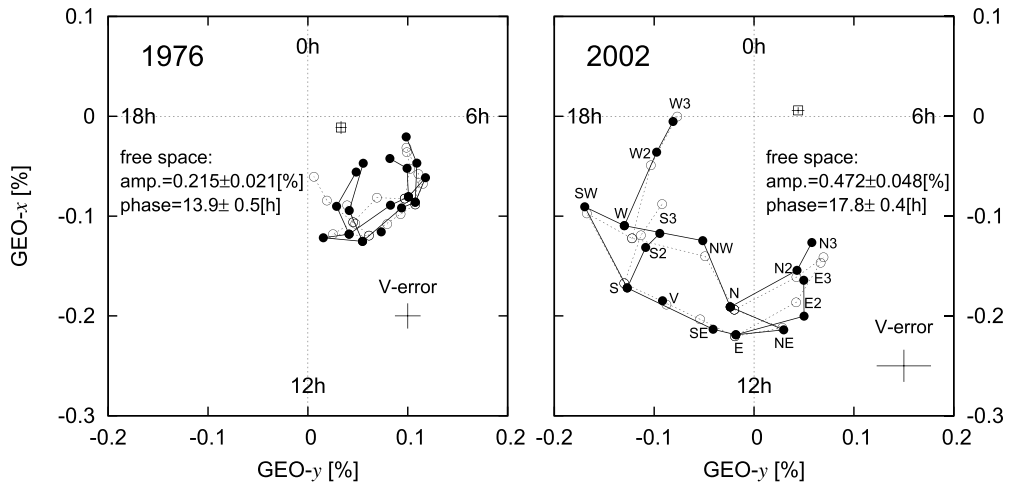

Figure 2. Yearly mean harmonic dials of the diurnal anisotropy observed by the Nagoya multi-directional muon detector in 1976 (left) around the $A > 0$ solar activity minimum and in 2002 (right) in the $A < 0$ epoch. Solid circles display the harmonic vector ($a_{1,j}^{1,\mathrm{obs}}$, $b_{1,j}^{1,\mathrm{obs}}$) observed by the jth directional channel with $a_{1,j}^{1,\mathrm{obs}}$ and $b_{1,j}^{1,\mathrm{obs}}$ plotted on the vertical (GEO-x) and horizontal (GEO-y) axes, respectively, while open circles display the best-fit vectors. The phases of the diurnal anisotropy with $x > 0$ and $y = 0$; $x = 0$ and $y > 0$; $x < 0$ and $y = 0$; and $x = 0$ and $y < 0$ are 00:00, 06:00, 12:00, and 18:00 hr in the local solar time, respectively. To demonstrate the relative configuration of the observed (best-fit) harmonic vectors in 17 directional channels, the head of each vector is connected with each other by solid (dotted) thin lines (see directional channels indicated in the right panel). An open square with an error cross in each panel displays the common vector representing the atmospheric temperature effect. The amplitude and phase of the best-fit harmonic vector in free space are indicated in each panel. For reference, the cross in the bottom right corner in each panel represents errors of $a_{1,j}^{1,\mathrm{obs}}$ and $b_{1,j}^{1,\mathrm{obs}}$ in the vertical (V) channel, deduced from the dispersion of monthly values.

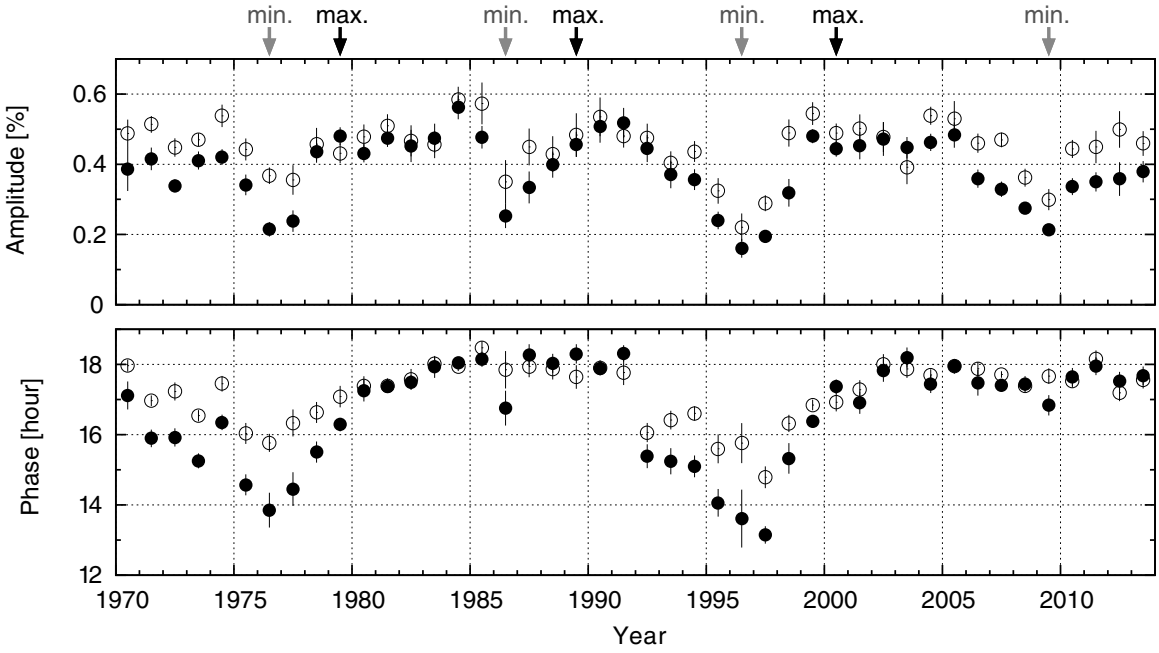

Figure 3. Diurnal anisotropy in free space. The yearly mean amplitude in % and the phase (denoted by the local solar time of the maximum intensity in hours) of the diurnal anisotropy are displayed in the upper and lower panels, respectively, each as a function of year on the horizontal axis. The solid and open circles display the anisotropy obtained from the MD data at 60 GV and from the NM data at 17 GV, respectively (see Table 2 in Appendix A for numerical data from the MD). The diurnal anisotropy in this figure is corrected for the Compton–Getting effect arising from the Earth's orbital motion around the Sun (see the text). The yearly mean and error are deduced from the means and dispersions of the monthly values, respectively. The solar maximum and minimum periods are indicated by black and gray arrows above the upper panel, respectively.

a_{com}^{T}, and b_{com}^{T} ($\xi_x^{\mathrm{GEO}(A)}$, $\xi_y^{\mathrm{GEO}(A)}$, a_{com}^{A}, and b_{com}^{A}) in the *toward* (*away*) sector in each month. Monthly mean parameters are then calculated by taking the mean of *toward* and *away* values.

For the following discussions of yearly mean parameters, we also assign the polarity of the large-scale solar magnetic field for each year, referring to the "Solar Polar Field Strength" available at the WSO Web site where the average polar field strength is given in every Carrington rotation. We assign the polarity of a year as $A > 0$ ($A < 0$) when the average polar field in the year is positive and pointing away from the Sun in the northern (southern) hemisphere. We regard a year as a period of the polarity reversal in progress when the year contains Carrington rotations with the polar field pointing *away* or *toward* in both hemispheres. For a period prior to 1975 when the WSO data are unavailable, we follow the assignment in Paper I. The polarity of each year assigned by us is indicated in Table 2 in Appendix A.

Figure 3 displays temporal variations of the amplitude (upper panel) and phase (lower panel) of the yearly mean harmonic vector in free space. Clearly seen in this figure is a phase in the lower panel showing a prominent 22 yr variation, with minima

occurring in 1976 and 1997 around $A > 0$ solar minima. This phase variation is ~2 hr in the NM data (open circles), and it is almost double (~4 hr) in the MD data (solid circles). The amplitude of the diurnal anisotropy in the upper panel is smaller (larger) around the solar minimum (maximum) period in both the NM and MD data. Table 2 in Appendix A lists numerical data of best-fit parameters obtained for each year. As shown in Figure 9 in Appendix A, the mean amplitude of the common vector $(a_{\rm com}, b_{\rm com})$ in Equations (8a) and (8b), which is introduced to represent the atmospheric temperature effect, is small (0.039% ± 0.002%), while the phase is almost stable around ~06:00 local time, in agreement with the average temperature effect reported from muon observations (e.g., Mori et al. 1998). It is also seen in Figure 9 that the common vector shows no notable long-term variations in correlation with the solar activity or magnetic cycle.

2.3.4. Derivation of the North–South Anisotropy

We derive the NS anisotropy perpendicular to the ecliptic plane at 60 GV from the Nagoya GG component (see Paper II for the derivation of the NS anisotropy from NM data). The GG component is a difference combination between intensities recorded in the north- and south-viewing channels designed to represent the NS anisotropy free from the atmospheric temperature effect (Nagashima et al. 1972; Mori & Nagashima 1979). The GG component is defined as

$$\mathrm{GG}(t) = \{r_{\rm N2}(t) - r_{\rm S2}(t)\} + \{r_{\rm N2}(t) - r_{\rm E2}(t)\}, \quad (11)$$

where $r_{XX}(t)$ is the percent deviation of the pressure-corrected muon rate $I_{XX}(t)$ in the directional channel XX(= N2, S2, E2) from the monthly mean. We calculate GG^T and GG^A by averaging GG(t) over *toward* and *away* days, respectively, according to the IMF sector polarity in every month and calculate the difference, ΔGG, as

$$\Delta\mathrm{GG} = (\mathrm{GG}^T - \mathrm{GG}^A)/2. \quad (12)$$

The NS anisotropy $\xi_z^{\mathrm{GEO}(T)}$ in space in the *toward* sector is calculated in every month from ΔGG as

$$\xi_z^{\mathrm{GEO}(T)} = \Delta\mathrm{GG}\big/\big(2c^0_{1,\mathrm{N2}} - c^0_{1,\mathrm{S2}} - c^0_{1,\mathrm{E2}}\big), \quad (13)$$

where $c^0_{1,XX}$ is the coupling coefficient for the directional channel XX, given as

$$c^0_{1,XX} = \frac{1}{\bar{I}_{XX}} \int_{p_{cXX}}^{\infty} \int_{\Omega_{XX}} \int_{S_{XX}} Y \cdot G(p) \cdot P_1^0(\cos\theta_{\rm or}) dS d\Omega dp \quad (14)$$

with the rigidity spectrum $G(p)$ in Equation (9). We deduce ξ_z^{GEO} from the difference between GG components in *toward* and *away* days (ΔGG) in Equation (12) because of the assumption that the anisotropy vector, when averaged over one month, is symmetric with respect to the HCS and the NS anisotropy lies in an opposite direction with the same magnitude above and below the HCS, as

$$\xi_z^{\mathrm{GEO}(A)} = -\xi_z^{\mathrm{GEO}(T)}. \quad (15)$$

2.4. Derivation of Modulation Parameters

2.4.1. Anisotropy Components in the Solar Wind Frame

Three components $(\xi_x^{\mathrm{GEO}(T/A)}, \xi_y^{\mathrm{GEO}(T/A)}, \xi_z^{\mathrm{GEO}(T/A)})$ of the space anisotropy vector obtained above are first converted to components $(\xi_x^{(T/A)}, \xi_y^{(T/A)}, \xi_z^{(T/A)})$ in the GSE and then transformed to the solar wind frame to derive the modulation parameters. We obtain the anisotropy components $(\xi_x^{\mathrm{SW}}, \xi_y^{\mathrm{SW}}, \xi_z^{\mathrm{SW}})$ in the solar wind frame by subtracting the contribution from the solar wind convection as

$$\xi_x^{\mathrm{SW}(T/A)} = \xi_x^{(T/A)} - (2+\Gamma)V_{\mathrm{SW}}^{(T/A)}/c \quad (16a)$$

$$\xi_y^{\mathrm{SW}(T/A)} = \xi_y^{(T/A)} \quad (16b)$$

$$\xi_z^{\mathrm{SW}(T/A)} = \xi_z^{(T/A)}, \quad (16c)$$

where $V_{\mathrm{SW}}^{(T/A)}$ is the radial component of the solar wind velocity in the omnitape data (King & Papitashvili 2005). We then calculate parallel and perpendicular components of the anisotropy as

$$\xi_{\parallel}^{(T/A)} = \xi_x^{\mathrm{SW}(T/A)} b_x^{(T/A)} + \xi_y^{\mathrm{SW}(T/A)} b_y^{(T/A)} \quad (17a)$$

$$\xi_{\perp}^{(T/A)} = -\xi_x^{\mathrm{SW}(T/A)} b_y^{(T/A)} + \xi_y^{\mathrm{SW}(T/A)} b_x^{(T/A)}, \quad (17b)$$

where $b_x^{(T/A)}$ and $b_y^{(T/A)}$ are GSE components of a unit vector pointing away from the Sun along the IMF and calculated from the mean IMF in the omnitape data. Note that positive $\xi_{\parallel}^{(T/A)}$ and $\xi_{\perp}^{(T/A)}$ correspond to the GCR streaming inward to the inner heliosphere parallel and perpendicular to the IMF, respectively. We finally obtain monthly average components of the anisotropy in the solar wind frame as

$$\xi_{\parallel} = \big(\xi_{\parallel}^{(T)} + \xi_{\parallel}^{(A)}\big)/2 \quad (18a)$$

$$\xi_{\perp} = \big(\xi_{\perp}^{(T)} + \xi_{\perp}^{(A)}\big)/2 \quad (18b)$$

$$\xi_z = \big(\xi_z^{(T)} - \xi_z^{(A)}\big)/2. \quad (18c)$$

This definition of ξ_z is again from the assumption of symmetry above and below the HCS. Note that a positive ξ_z corresponds to the southward GCR streaming perpendicular to the ecliptic plane in the *toward* IMF sector. We perform calculations of $\xi_{\parallel}$, $\xi_{\perp}$, ξ_z described above in each month and deduce the yearly mean value and its error for each anisotropy component from the mean and dispersion of 12 monthly values, respectively. Figure 4 shows $\xi_{\parallel}$, $\xi_{\perp}$, ξ_z each as a function of year. It is seen that three components of the anisotropy derived from MD data (solid circles) are all positive throughout the entire period in this figure. A clear 22 yr variation seen in $\xi_{\parallel}$ in Figure 4(a) indicates that this component anisotropy is responsible for the phase variation in Figure 3, as discovered in Papers I and II. No such clear signature of 22 yr variation is seen in either $\xi_{\perp}$ or ξ_z, displayed in Figures 4(b) and (c).

There is a close correlation between the variation of the $\xi_{\parallel}$ values obtained for NMs at 17 GV and for the MD at 60 GV (open and solid circles in Figure 4(a), respectively), indicating a weak rigidity dependence of this anisotropy component. A scatter plot of $\xi_{\parallel}$ for NMs and for the MD on the x and y axes, respectively, yields a correlation coefficient $r = 0.92$ and a slope (ratio) of $y/x = \beta = 0.89 \pm 0.05$, which suggests that $\xi_{\parallel}$ remains nearly constant despite the factor of 3.5 difference between the rigidity ranges monitored by the NM and MD. On the other hand, we find $\beta = 0.77 \pm 0.07$ for $A > 0$, which is significantly smaller than the value of $\beta = 0.94 \pm 0.05$ found for the $A < 0$ epochs, showing that the rigidity spectrum of $\xi_{\parallel}$ is softer in the $A > 0$ epochs. We also see a remarkable correlation between $\xi_{\perp}$ for NMs and for the MD with $r = 0.75$,

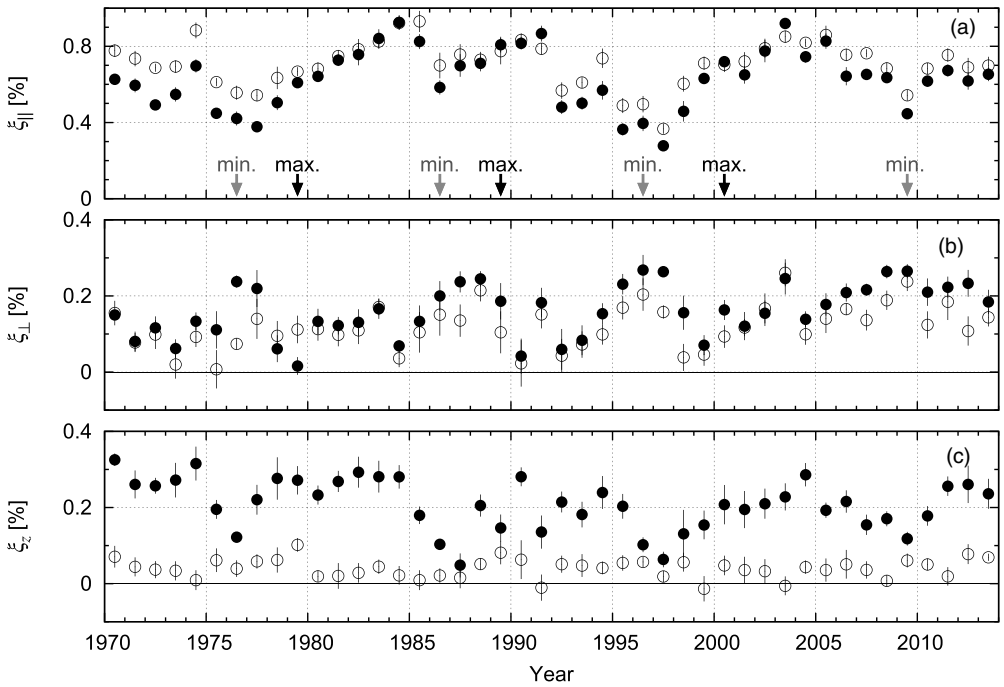

Figure 4. Three components of the anisotropy in the solar wind frame. Each panel from top to bottom displays the yearly mean $\xi_\parallel$, $\xi_\perp$, and ξ_z in percentages as a function of year. Solid circles display the anisotropy components derived from the MD data at 60 GV, while open circles show the anisotropy derived from the NM data at 17 GV (see Table 2 in Appendix A for numerical data from the MD). The yearly mean and error are deduced from the means and dispersions of the monthly values, respectively. The solar maximum and minimum periods are indicated by black and gray arrows on the horizontal axis of the top panel, respectively.

while the β values turn out to be 1.65 ± 0.35 (1.26 ± 0.14) in $A > 0$ ($A < 0$) epochs, which indicates that $\xi_\perp$ increases with increasing P_m. The most significant difference between NM and MD data is seen in the magnitude of ξ_z shown in Figure 4(c). For this component, we obtain $\beta = 4.45 \pm 0.61$ (6.08 ± 0.96) for the $A > 0$ ($A < 0$) epochs, which implies that ξ_z increases with increasing rigidity. The correlation between NM and MD data is, however, quite poor ($r = 0.20$) for this component. These features appearing in Figure 4 are qualitatively consistent with $\xi_\perp$ and ξ_z increasing with rigidity. The ratios β for the three anisotropy components are listed in the column "$P_u = 100$ GV" in Table 3 in Appendix B.

We cannot derive any quantitative conclusions about the rigidity spectrum of the anisotropy from the present analysis, which assumes a priori a flat spectrum with the upper limiting rigidity P_u fixed at 100 GV as denoted in Equation (9). Each value of the ratios (βs) described above, for instance, changes for a different value of P_u. The rigidity dependences of $\xi_\parallel$, $\xi_\perp$, and ξ_z relative to each other, however, remain unchanged even for different values of P_u (see Appendix B). We will discuss the physical origin of these rigidity dependences in the next subsection.

2.4.2. Modulation Parameters

Three components ($\xi_\parallel$, $\xi_\perp$, ξ_z) of the anisotropy vector in the solar wind frame obtained above are related to the modulation parameters, i.e., the spatial gradients of GCR density and mean free paths of the pitch angle scattering of GCRs in the turbulent magnetic field, as

$$\xi_\parallel = \lambda_\parallel G_r \cos\psi \tag{19a}$$

$$\xi_\perp = \lambda_\perp G_r \sin\psi - R_L G_z \tag{19b}$$

$$\xi_z = R_L G_r \sin\psi + \lambda_\perp G_z, \tag{19c}$$

where $\lambda_\parallel$ and $\lambda_\perp$ are mean free paths of the pitch angle scattering parallel and perpendicular to the IMF, respectively, R_L is the Larmor radius of GCRs in the IMF, and ψ is the IMF spiral angle between the radial direction and a unit vector **b** in Equations (17a) and (17b) pointing away from the Sun along the IMF. G_r and G_z are the radial and latitudinal components of the fractional density gradient vector, defined as

$$\mathbf{G} = \nabla U / U, \tag{20}$$

where U is the GCR density (or omnidirectional intensity) given as a function of the position in the heliosphere, time, and GCR rigidity. We assume that the longitudinal gradient is zero in our analyses based on the anisotropy averaged over one month, which is longer than the solar rotation period. Note that G_z represents the latitudinal density gradient in the *toward* sector, as it is positive when U increases with increasing latitude, and changes its sign in the *away* sector due to the assumed symmetry above and below the HCS. The bi-directional latitudinal density gradient $G_{|z|}$, which is defined to be positive (negative) when U increases away from (toward) the HCS, is given by G_z as

$$G_{|z|} = -\mathrm{sgn}(A) G_z, \tag{21}$$

where A represents the polarity of the solar dipole magnetic moment and

$$\begin{aligned} \mathrm{sgn}(A) &= +1, \quad \text{for } A > 0 \text{ epoch}, \\ &= -1, \quad \text{for } A < 0 \text{ epoch}. \end{aligned}$$

Equations (19a)–(19c) include four unknown modulation parameters, $\lambda_\parallel$, $\lambda_\perp$, G_r, and G_z, while we have only three components ($\xi_\parallel$, $\xi_\perp$, ξ_z) of the observed anisotropy. We therefore assume in this paper

$$\lambda_\perp / \lambda_\parallel = \alpha = 0.01 \tag{22}$$

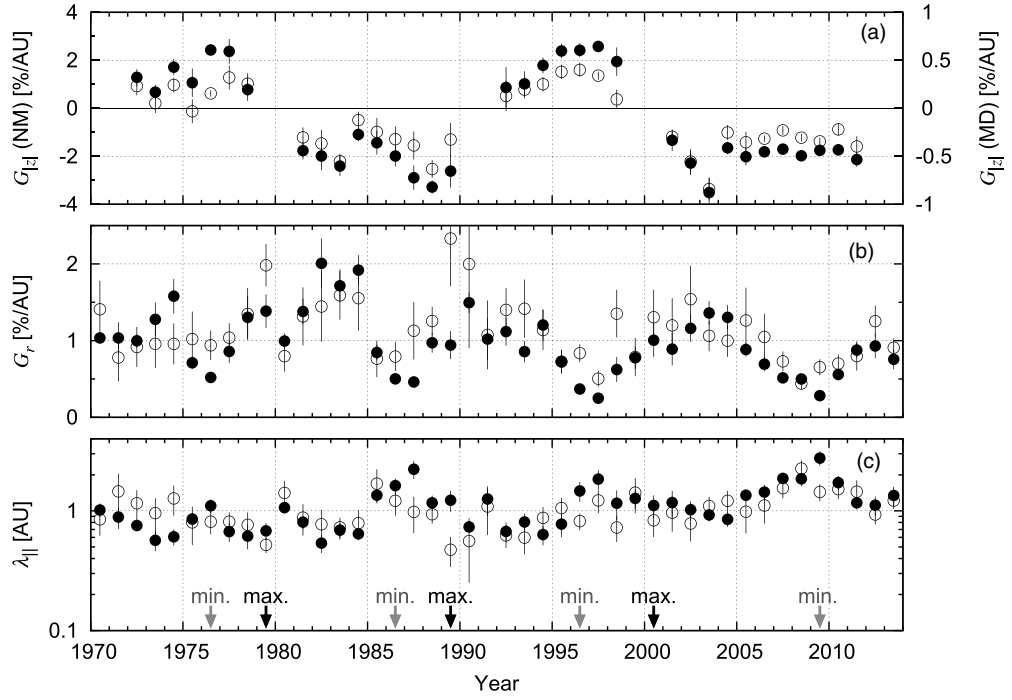

Figure 5. Modulation parameters derived from the 3D anisotropy. Each panel from top to bottom displays the yearly mean $G_{|z|}$, G_r, and $\lambda_\parallel$, each as a function of year. Solid circles display parameters derived from the MD data at 60 GV, while open circles show parameters derived from the NM data at 17 GV (see Table 2 in Appendix A for numerical data from the MD). Note that the bi-directional latitudinal density gradient ($G_{|z|}$) in the top panel is defined to be positive (negative) when the spatial distribution of the GCR density has a local minimum (maximum) on the HCS. $G_{|z|}$ and G_r in the top and middle panels are plotted on the vertical axis in linear scales, while $\lambda_\parallel$ in the bottom panel is plotted in a logarithmic scale. The yearly mean and error are deduced from the means and dispersions of the monthly values, respectively. Because of the definition in Equation (21), $G_{|z|}$ is not available in a year when the polarity reversal is in progress. The solar maximum and minimum periods are indicated by black and gray arrows on the horizontal axis of the bottom panel, respectively.

and derive three remaining parameters, $\lambda_\parallel$, G_r, and G_z. Papers I and II also adopted the same constant value of α based on empirical determinations of $\lambda_\parallel \approx 0.5$ AU by Bieber & Pomerantz (1983) and $\lambda_\perp \approx 0.007$ AU by Palmer (1982) for ~10 GV GCRs. From Equation (19a), we get

$$G_r = \xi_\parallel / \left(\lambda_\parallel \cos\psi\right). \tag{23}$$

Introducing this into Equation (19b), we get

$$G_z = \left(\alpha\xi_\parallel \tan\psi - \xi_\perp\right)/R_L. \tag{24}$$

From Equation (19a), on the other hand, we also get

$$\lambda_\parallel = \xi_\parallel / \left(G_r \cos\psi\right). \tag{25}$$

Introducing Equations (24) and (25) into Equation (19c), we get a quadratic equation for G_r:

$$R_L \sin\psi G_r^2 - \xi_z G_r - \alpha\xi_\parallel(\xi_\perp - \alpha\xi_\parallel \tan\psi)/(R_L \cos\psi) = 0, \tag{26}$$

which has a solution for positive G_r of

$$G_r = \{\xi_z + \sqrt{\xi_z^2 + 4\alpha\xi_\parallel \tan\psi(\xi_\perp - \alpha\xi_\parallel \tan\psi)}\}/(2R_L \sin\psi). \tag{27}$$

We first calculate $G_{|z|}$ and G_r from Equations (24) and (27), respectively, for every month. We then deduce the yearly mean and its error for each parameter from the means and dispersions of 12 monthly values, respectively. We do not use Equation (25) to calculate the monthly value of $\lambda_\parallel$ because G_r, particularly as derived from NM data, becomes close to zero in some months, resulting in an extremely large $\lambda_\parallel$ and large error of the yearly mean $\lambda_\parallel$. We instead derive the yearly mean $\lambda_\parallel$ from the yearly mean G_r and $\cos\psi$ in Equation (25) and deduce the error by propagating from the errors of the yearly mean G_r and $\cos\psi$. For R_L in the MD and NM data, we use gyro-radii of 60 GV and 17 GV GCRs, respectively, in the monthly mean IMF with the magnitude calculated from the omnitape data.

Figure 5 shows the temporal variations of the calculated modulation parameters, $G_{|z|}$, G_r, and $\lambda_\parallel$. We can clearly see in Figure 5(a) that the bi-directional latitudinal density gradient ($G_{|z|}$) is positive (indicating the local density minimum on the HCS) in the $A > 0$ epoch, while it is negative (indicating the local density maximum on the HCS) in the $A < 0$ epoch, in agreement with the drift model prediction (Kóta & Jokipii 1983). There is no clear signature of an 11 yr variation in $G_{|z|}$. The 22 yr variation of $G_{|z|}$ appears cleaner and statistically more significant with relatively smaller errors in the MD data than in the NM data. The mean $G_{|z|}$ derived from the MD (NM) data is 0.42 ± 0.05 (0.86 ± 0.14)% AU^{-1} in $A > 0$, while it is -0.52 ± 0.04 (-1.47 ± 0.15)% AU^{-1} in $A < 0$, indicating that the magnitude of $G_{|z|}$ is larger in $A < 0$ than in $A > 0$ in both the MD and NM data.

The radial density gradient (G_r) in Figure 5(b), on the other hand, varies with a ~11 yr solar activity cycle with maxima (minima) in solar maximum (minimum) periods (Papers I and II; Bieber & Pomerantz 1986), but there is no significant difference seen between mean G_r in $A > 0$ and $A < 0$ epochs. The mean G_r deduced from the MD (NM) data is 0.89 ± 0.11 (1.04 ± 0.08)% AU^{-1} in the $A > 0$ epoch, while it is 0.99 ± 0.12 (1.13 ± 0.10)% AU^{-1} in the $A < 0$ epoch. It is noted that we find a poor correlation between temporal variations of $G_{|z|}$ and G_r in both the NM and muon data.

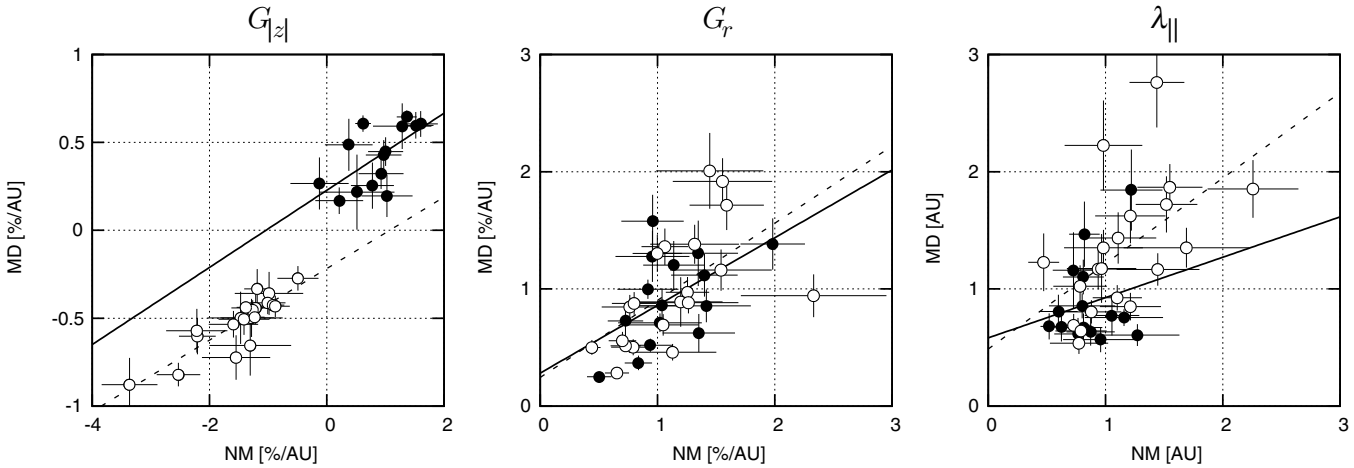

Figure 6. Correlation plots between modulation parameters derived from the NM data at 17 GV and the MD data at 60 GV. The left, middle, and right panels show correlations of $G_{|z|}$, G_r, and $\lambda_{||}$, respectively. Each panel displays the parameter in Figure 5 derived from the MD data at 60 GV on the vertical axis as a function of the parameter derived from the NM data at 17 GV in the same year on the horizontal axis. Solid and open circles in each panel display parameters in the $A > 0$ and $A < 0$ epochs, respectively. Data points in years when the polarity reversal is in progress are omitted in this figure.

The parallel mean free path ($\lambda_{\parallel}$) in Figure 5(c) also changes with the solar activity cycle with minima (maxima) in solar maximum (minimum) periods. The mean $\lambda_{\parallel}$ deduced from the MD (NM) data is 0.90 ± 0.10 (0.89 ± 0.06) AU in $A > 0$, while it is 1.32 ± 0.13 (1.14 ± 0.10) AU in $A < 0$. This indicates that the mean $\lambda_{\parallel}$ is systematically larger in $A < 0$ than in $A > 0$ at the 2 or 3 sigma level. It is also interesting that $\lambda_{\parallel}$ in the NM and MD data appear to be persistently increasing toward maxima in 2008 and 2009 during the last three solar activity cycles, while G_r appear to be decreasing. The parallel mean free path ($\lambda_{\parallel}$) deduced from the NM data (open circles) shows peaks in 1985 and 2008 in $A < 0$ solar minimum epochs, while it shows smaller peaks in 1974 and 1997 in $A > 0$ solar minimum epochs. This is qualitatively consistent with results reported in Paper I. In $\lambda_{\parallel}$ deduced from the MD data (solid circles), on the other hand, the 11 yr variation is more prominent with maxima in every solar minimum in 1976, 1987, 1997, and 2009, but no clear 22 yr variation is visible in this figure. We will discuss long-term variations of G_r and $\lambda_{\parallel}$ in more detail in the next section.

We now discuss the rigidity dependence of each modulation parameter. Figure 6 shows the correlation between the parameters derived from the NM data at 17 GV and from the MD data at 60 GV. In the $A > 0$ ($A < 0$) epoch, $G_{|z|}$ from the NM and MD data in the left panel shows a good correlation with r of 0.63 (0.86), while the mean ratio ($\beta = y/x$) of $G_{|z|}$ from the MD data to that from the NM data is 0.48 ± 0.10 (0.35 ± 0.05) in the $A > 0$ ($A < 0$) epoch, indicating that $G_{|z|}$ decreases with increasing P_m. Similar but weaker correlations are also seen in G_r and $\lambda_{\parallel}$ in the middle and right panels, with an average r of 0.53 (0.58) and 0.21 (0.54), respectively, while the mean β of G_r and $\lambda_{\parallel}$ are 0.85 ± 0.12 (0.87 ± 0.13) and 1.00 ± 0.13 (1.16 ± 0.15), respectively, indicating that these parameters are almost independent of P_m. Note that β of $G_{|z|}$ is significantly smaller than β of G_r indicating the softer rigidity dependence of $G_{|z|}$ than that of G_r when P_u is fixed at 100 GV. The ratios β derived from different P_u are listed in Table 3 in Appendix B.

We finally discuss the physical origin of the rigidity dependence of each anisotropy component presented in the preceding subsection. As expressed in Equations (19a)–(19c), $\xi_{\perp}$ and ξ_z include contributions from the drift (i.e., the diamagnetic drift) added to the perpendicular diffusion, while $\xi_{\parallel}$ results solely from the parallel diffusion. Using G_r, $G_{|z|}$, and $\lambda_{\parallel}$ with an assumption of $\lambda_{\perp} = \alpha\lambda_{\parallel} = 0.01\lambda_{\parallel}$, we calculate individual contributions from the diffusion and drift to each of $\xi_{\perp}$ and ξ_z. We find that the mean diffusion contribution ($\lambda_{\perp} G_r \sin\psi$) to $\xi_{\perp}$ is significantly smaller than the mean drift contribution ($-R_L G_z$) in both the NM and MD data, hence $\xi_{\perp}$ is mainly arising from the drift effect. The mean ratio of $|\lambda_{\perp} G_r \sin\psi|$ to $|-R_L G_z|$ contributing to $\xi_{\perp}$ is 0.08 ± 0.02 in the NM data, while the ratio is 0.07 ± 0.02 in the MD data, indicating that the mean contribution from the diffusion to $\xi_{\perp}$ is less than 10% in both the NM and MD data, independent of P_m. The mean ratio of the diffusion ($|\lambda_{\perp} G_z|$) to the drift ($|R_L G_r \sin\psi|$) contributing to ξ_z is also small in the MD data, 0.03 ± 0.01. The ratio in the NM data, on the other hand, is 0.19 ± 0.03 and significantly larger than the ratio in the MD data, indicating that the relative contribution of the diffusion to ξ_z increases with decreasing P_m. This is due to the rigidity dependence of $G_{|z|}$, which is softer than that of G_r, as discussed above. Since there is only a poor correlation between temporal variations of $G_{|z|}$ and G_r in Figure 5, this may explain the poor correlation between ξ_z in the NM and MD data, which is shown in the bottom panel of Figure 4 and discussed in the preceding subsection.

3. SUMMARY AND DISCUSSIONS

We examined the energy dependence of long-term variations in the 3D anisotropy of GCR intensity by analyzing the data recorded in 1970–2013 by NMs (Swarthmore/Newark, Alert/Thule, and McMurdo) that have median responses to ~17 GV primary GCRs and the Nagoya MD that has the median response to ~60 GV GCRs. The derived free-space harmonic vector of the diurnal anisotropy changes its phase to earlier hours in $A > 0$ solar minima from the ~18:00 local time known as the phase of the "corotation" anisotropy, while the amplitude changes in an 11 yr cycle, decreasing to a small value in the years around every solar minimum. We note that the magnitude of the phase change is significantly larger in the MD data than in the NM data, indicating a marked rigidity dependence of the phase change. A clear 22 yr variation is seen in the parallel component ($\xi_{\parallel}$) of the anisotropy, confirming the conclusion of Paper II that $\xi_{\parallel}$ is primarily responsible for the phase change. The NS anisotropy (ξ_z) derived from the GG component of the Nagoya MD also

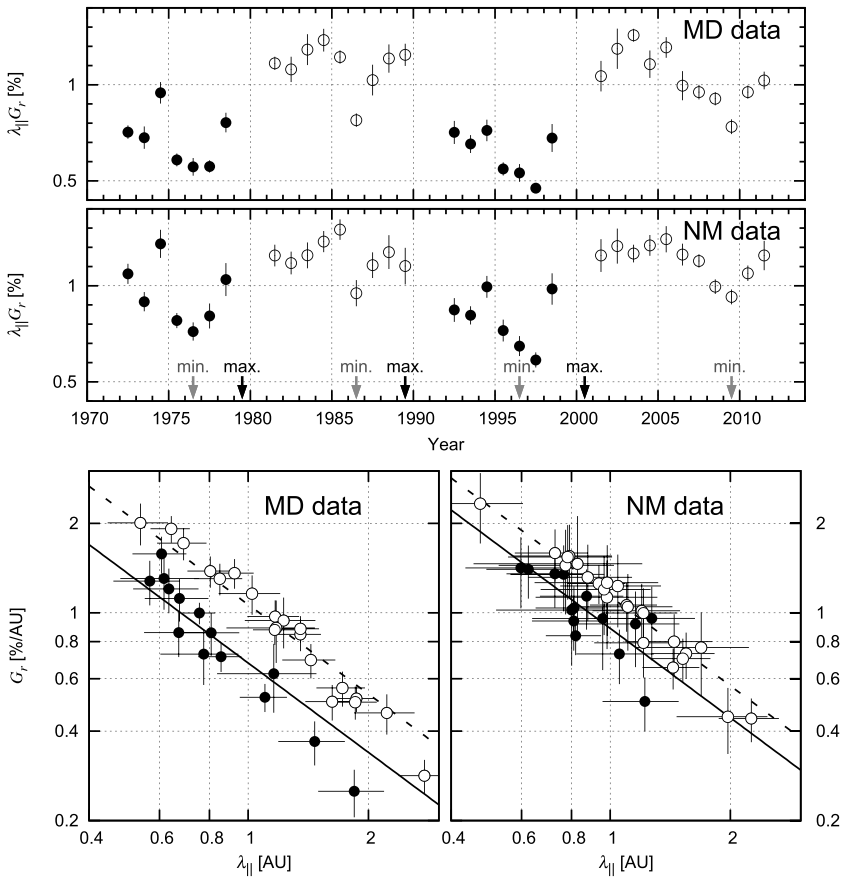

Figure 7. Temporal variation of $\lambda_\parallel G_r$ and the correlation between G_r and $\lambda_\parallel$. The upper two panels display yearly mean $\lambda_\parallel G_r$ calculated from $\xi_\parallel / \cos\psi$, each as a function of year. The top panel shows $\lambda_\parallel G_r$ deduced from the MD data, while the middle panel shows $\lambda_\parallel G_r$ deduced from the NM data. Yearly mean values in the $A > 0$ ($A < 0$) epoch are displayed as solid (open) circles, each with an error deduced from the dispersion of monthly values in each year. Data points in years when the polarity reversal is in progress are omitted in this figure. The solar maximum and minimum periods are indicated by black and gray arrows on the horizontal axis of the middle panel, respectively. The bottom two panels are scatter plots between G_r and $\lambda_\parallel$ in logarithmic scales derived from the MD data (left) and the NM data (right). In each panel, the yearly mean G_r on the vertical (y) axis is plotted as a function of $\lambda_\parallel$ on the horizontal (x) axis. Solid and dashed straight lines display the functions $y = c/x$ with a constant parameter c best-fit to data in the $A > 0$ and $A < 0$ epochs, respectively.

shows an 11 yr cycle with minima in the years around every solar minimum.

The ecliptic anisotropy components ($\xi_\parallel$ and $\xi_\perp$) derived from the NM and MD data vary in close correlation with each other, while no such correlation is seen in the variation of ξ_z. The mean ratio between $\xi_\parallel$ in the MD and that in the NM data is roughly consistent with a rigidity-independent spectrum, while the rigidity spectrum of $\xi_\parallel$ is systematically softer in $A > 0$ than in $A < 0$. On the other hand, $\xi_\perp$ and ξ_z derived from the MD data are significantly larger than those from the NM data, indicating that these components increase with P_m. According to Equations (19a)–(19c), $\xi_\perp$ and ξ_z include contributions from the gyration of particles (connected to diamagnetic drift) added to perpendicular diffusion, while $\xi_\parallel$ is caused by the parallel diffusion alone. It is reasonable, therefore, to expect that the observed harder rigidity spectra of $\xi_\perp$ and ξ_z are due to effects from drift. Based on numerical simulations of particle propagation in the turbulent magnetic field, Minnie et al. (2007) has shown that drifts are suppressed by magnetic turbulence, but the suppression sets in at lower turbulence amplitudes for low-energy cosmic rays than for high-energy cosmic rays. This may give a possible explanation for why the contribution of drift streaming results in a harder rigidity spectrum. If this is the case, we may well need two different spectra, representing diffusion and drift, combined in $\xi_\perp$ and ξ_z, to reproduce the correct rigidity dependence of the diurnal anisotropy in space. We will present such analyses elsewhere.

Equations (19a)–(19c) also imply that the drift contribution to $\xi_\perp$ is proportional to $G_{|z|}$, while the drift contribution to ξ_z is proportional to G_r. By comparing G_r and $G_{|z|}$ derived from the NM and MD data, we find that the rigidity dependences of G_r and ξ_z are harder than those of $G_{|z|}$ and $\xi_\perp$. Yasue (1980) and Hall et al. (1994) analyzed the NS anisotropy observed with NMs and MDs monitoring a wide range of P_m and found ξ_z increasing with the rigidity up to several hundred GV. This is in qualitative agreement with this paper.

We finally discuss the long-term variations of the modulation parameters. Figure 7 shows the temporal variation of $\lambda_\parallel G_r = \xi_\parallel / \cos\psi$ (see Equation (19a)). We can clearly see that the mean magnitude of $\lambda_\parallel G_r$ is significantly smaller in $A > 0$ (solid circles) than in $A < 0$ periods (open circles). The mean magnitudes of $\lambda_\parallel G_r$ derived from the MD data and that from the NM data in the $A < 0$ epoch are $1.07\% \pm 0.03\%$ and $1.14\% \pm 0.02\%$, respectively, which are fairly consistent with each other. The mean magnitudes in $A > 0$ periods are $0.68\% \pm 0.04\%$ and $0.89\% \pm 0.05\%$, respectively. Combined with the solar wind convection, this reduction of $\lambda_\parallel G_r$ results in the observed phase shift of the diurnal anisotropy to earlier hours in $A > 0$, as suggested by Paper I. We also note that the ratio of $\lambda_\parallel G_r$ for the MD to that for NM data is smaller in $A > 0$

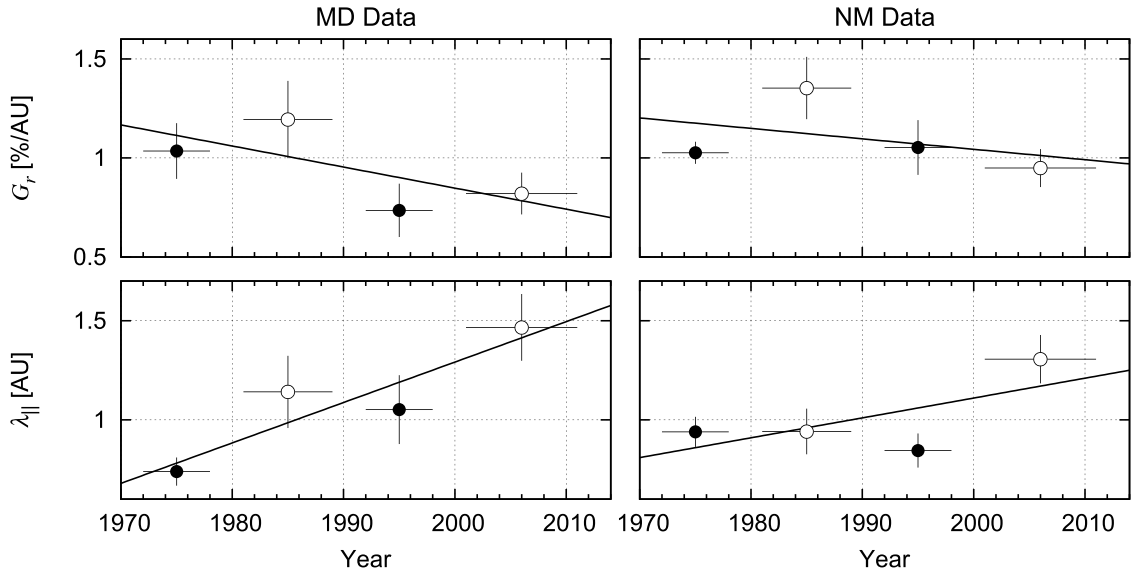

Figure 8. Long-term trends of mean G_r and $\lambda_\parallel$ in each solar magnetic polarity epoch. The left (right) two panels display means derived from the MD (NM) data. Means in the $A > 0$ and $A < 0$ epochs are plotted as solid and open circles, respectively, at the central year of each epoch. The vertical error is deduced from the dispersion of yearly means in each epoch, while the horizontal bar indicates the period included in each epoch. The solid straight line in each panel displays the linear long-term trend best fit to four data points.

than in $A < 0$ periods, indicating a softer rigidity spectrum of this component for $A > 0$ than for $A < 0$ (see the discussion of Figure 4 in the preceding section). This decrease in $\lambda_\parallel G_r$ in the $A > 0$ epoch, which is larger in the MD data than in the NM data, is responsible for the larger phase shift of the diurnal anisotropy in the $A > 0$ solar minimum epoch in the MD data. The rigidity spectrum of $\xi_\perp$, which is harder than that of $\xi_\parallel$ mentioned above, is also partly responsible for the larger phase shift in the MD data in $A > 0$ minimum epochs. Hall et al. (1997) used the NM and MD data to analyze the rigidity spectrum of the diurnal anisotropy and obtained the average $G(p)$ proportional to $p^{-0.1\pm0.2}$ with $P_u = 100 \pm 25$ GV. Although their spectrum seems to be consistent with the $G(p)$ assumed in this paper, such a common spectrum for $\xi_\parallel$ and $\xi_\perp$ cannot reproduce the observed feature that the phase shift observed by MD in the $A > 0$ solar minimum epoch is significantly larger than that by NM.

The 11 and 22 yr variations are also apparent in the modulation parameters shown in Figure 5. The bi-directional latitudinal density gradient ($G_{|z|}$) in the top panel is positive (negative) in the $A > 0$ ($A < 0$) epoch in agreement with the drift model prediction of the local minimum (maximum) of GCR density around the HCS. This 22 yr variation looks more significant in the MD data than in the NM data, with a smaller error for each data point. The mean magnitude of $G_{|z|}$ is larger in $A < 0$ than in $A > 0$ in both the MD and NM data. The 11 yr variation is evident in the radial density gradient (G_r) in the middle panel of Figure 5, while we cannot identify a clear 22 yr variation, as reported by Bieber & Pomerantz (1986). The mean G_r deduced from the MD (NM) data is 0.89 ± 0.11 (1.04 ± 0.08)% AU^{-1} in the $A > 0$ epoch, while it is 0.99 ± 0.12 (1.13 ± 0.10)% AU^{-1} in the $A < 0$ epoch. Note that we find a poor correlation between temporal variations of $G_{|z|}$ and G_r in both the MD and NM data.

The mean parallel mean free path ($\lambda_\parallel$), on the other hand, turns out to be significantly larger in the $A < 0$ than in the $A > 0$ epoch, in both the MD and NM data. We find that the mean $\lambda_\parallel$ deduced from the MD (NM) data is 0.90 ± 0.10 (0.89 ± 0.06) AU in $A > 0$, while it is 1.32 ± 0.13 (1.14 ± 0.10) AU in $A < 0$. Paper I suggested that the 22 yr variation of $\lambda_\parallel$ is responsible for the reduction of $\lambda_\parallel G_r$ in $A > 0$ and for the 22 yr variation of the diurnal anisotropy. The two bottom panels of Figure 7 show the correlation between G_r and $\lambda_\parallel$ (both in logarithmic scale) on the vertical (y) and horizontal (x) axes, respectively. Since $\lambda_\parallel$ on the x-axis is deduced from $\lambda_\parallel G_r$ divided by G_r on the y-axis, data points in this scatter plot align on a straight line when $\lambda_\parallel G_r$ is constant during the analysis period. Solid and dashed straight lines in each panel display functions of $y = c/x$ best-fit to data in the $A > 0$ and $A < 0$ epochs, respectively, each with the intercept c as a best-fit parameter. It is seen that, for the MD data (left panel), the best-fit c for the $A > 0$ data (solid circles) is about 64% of that for the $A < 0$ data (open circles). This is consistent with the lower $\lambda_\parallel$ value derived from the MD data for $A > 0$ epochs, which is 68% (=0.90/1.32) of that in the $A < 0$ epoch, indicating that the 22 yr variation of $\lambda_\parallel G_r$ in the left panel is due to the 22 yr variation of $\lambda_\parallel$ on the horizontal axis.

However, as mentioned in connection with Figure 5 in the preceding section, we also find that $\lambda_\parallel$s (G_rs) from the NM and MD data appear to persistently increase (decrease) during the last three solar activity cycles, reaching maximum (minimum) in 2008–2009. Figure 8 displays the mean G_r and $\lambda_\parallel$ in the $A > 0$ and $A < 0$ epochs, each as a function of time. It is clear particularly in the MD data (left panels) that there is a long-term trend indicated by a best-fit solid line in each panel. This trend enhances the difference between the $A > 0$ and $A < 0$ means of $\lambda_\parallel$, while it reduces the difference between the means of G_r. The simple means of G_r or $\lambda_\parallel$ in all $A > 0$ and $A < 0$ epochs are, therefore, seriously biased by these long-term trends. If we look at the deviation of each data point from the solid line in the MD data, on the other hand, we find that G_r and $\lambda_\parallel$ are both larger (smaller) in the $A < 0$ ($A > 0$) epoch, although only at the 1σ level.

The phase shift of the diurnal anisotropy toward earlier hours in the $A > 0$ epochs is a robust consequence of particle drifts in the inhomogeneous large-scale heliospheric magnetic fields (HMFs). The observed phase shift in the $A > 0$ epoch arises naturally in various drift models employing different approaches

Table 2
Anisotropy Components and Modulation Parameters Derived from the Nagoya MD Data

year	sgn(A)[a]	Amplitude (%)	Phase (hr)	$\xi_{\parallel}$ (%)	$\xi_{\perp}$ (%)	ξ_z (%)	$G_{\|z\|}$ (%/AU)	G_r (%/AU)	$\lambda_{\parallel}$ (AU)
1970	*	0.39 ± 0.07	17.1 ± 0.4	0.63 ± 0.01	0.15 ± 0.01	0.33 ± 0.02	*	1.03 ± 0.05	1.02 ± 0.14
1971	*	0.42 ± 0.04	15.9 ± 0.3	0.60 ± 0.04	0.08 ± 0.03	0.26 ± 0.04	*	1.03 ± 0.21	0.89 ± 0.19
1972	+	0.34 ± 0.02	15.9 ± 0.3	0.49 ± 0.03	0.12 ± 0.04	0.26 ± 0.03	0.32 ± 0.09	1.00 ± 0.09	0.76 ± 0.08
1973	+	0.41 ± 0.03	15.3 ± 0.3	0.55 ± 0.04	0.06 ± 0.03	0.27 ± 0.05	0.17 ± 0.08	1.28 ± 0.22	0.57 ± 0.11
1974	+	0.42 ± 0.03	16.3 ± 0.3	0.70 ± 0.04	0.13 ± 0.03	0.32 ± 0.05	0.43 ± 0.09	1.58 ± 0.23	0.61 ± 0.10
1975	+	0.34 ± 0.03	14.6 ± 0.3	0.45 ± 0.02	0.11 ± 0.05	0.20 ± 0.03	0.27 ± 0.15	0.71 ± 0.08	0.86 ± 0.11
1976	+	0.21 ± 0.03	13.9 ± 0.5	0.42 ± 0.04	0.24 ± 0.02	0.12 ± 0.02	0.61 ± 0.05	0.52 ± 0.06	1.10 ± 0.15
1977	+	0.24 ± 0.04	14.5 ± 0.5	0.38 ± 0.03	0.22 ± 0.05	0.22 ± 0.04	0.59 ± 0.13	0.86 ± 0.15	0.67 ± 0.13
1978	+	0.44 ± 0.04	15.5 ± 0.4	0.50 ± 0.04	0.06 ± 0.04	0.28 ± 0.06	0.20 ± 0.13	1.30 ± 0.28	0.62 ± 0.14
1979	*	0.48 ± 0.03	16.3 ± 0.2	0.61 ± 0.03	0.02 ± 0.03	0.27 ± 0.04	*	1.38 ± 0.22	0.68 ± 0.12
1980	*	0.43 ± 0.03	17.3 ± 0.4	0.64 ± 0.03	0.13 ± 0.04	0.23 ± 0.03	*	0.99 ± 0.11	1.06 ± 0.12
1981	−	0.47 ± 0.03	17.4 ± 0.2	0.73 ± 0.04	0.12 ± 0.03	0.27 ± 0.03	−0.44 ± 0.10	1.38 ± 0.17	0.80 ± 0.10
1982	−	0.45 ± 0.05	17.5 ± 0.3	0.76 ± 0.06	0.13 ± 0.04	0.29 ± 0.05	−0.50 ± 0.15	2.01 ± 0.33	0.54 ± 0.10
1983	−	0.47 ± 0.05	17.9 ± 0.4	0.84 ± 0.05	0.17 ± 0.03	0.28 ± 0.05	−0.60 ± 0.11	1.72 ± 0.22	0.69 ± 0.10
1984	−	0.56 ± 0.04	18.0 ± 0.2	0.92 ± 0.04	0.07 ± 0.02	0.28 ± 0.04	−0.27 ± 0.07	1.92 ± 0.20	0.64 ± 0.08
1985	−	0.48 ± 0.04	18.1 ± 0.3	0.82 ± 0.04	0.13 ± 0.05	0.18 ± 0.03	−0.36 ± 0.13	0.85 ± 0.11	1.35 ± 0.17
1986	−	0.25 ± 0.04	16.8 ± 0.5	0.58 ± 0.04	0.20 ± 0.04	0.10 ± 0.02	−0.50 ± 0.11	0.50 ± 0.07	1.62 ± 0.24
1987	−	0.33 ± 0.05	18.3 ± 0.4	0.70 ± 0.06	0.24 ± 0.03	0.05 ± 0.04	−0.72 ± 0.13	0.46 ± 0.08	2.22 ± 0.39
1988	−	0.40 ± 0.04	18.0 ± 0.3	0.71 ± 0.05	0.24 ± 0.03	0.21 ± 0.03	−0.82 ± 0.07	0.97 ± 0.13	1.17 ± 0.18
1989	−	0.46 ± 0.04	18.3 ± 0.3	0.81 ± 0.05	0.19 ± 0.05	0.15 ± 0.04	−0.65 ± 0.18	0.94 ± 0.19	1.23 ± 0.25
1990	*	0.51 ± 0.05	17.9 ± 0.2	0.82 ± 0.04	0.04 ± 0.05	0.28 ± 0.03	*	1.49 ± 0.14	0.73 ± 0.08
1991	*	0.52 ± 0.05	18.3 ± 0.3	0.87 ± 0.05	0.18 ± 0.04	0.14 ± 0.05	*	1.02 ± 0.28	1.25 ± 0.35
1992	+	0.45 ± 0.04	15.4 ± 0.4	0.48 ± 0.04	0.06 ± 0.06	0.21 ± 0.03	0.22 ± 0.22	1.12 ± 0.19	0.67 ± 0.13
1993	+	0.37 ± 0.04	15.2 ± 0.4	0.50 ± 0.04	0.08 ± 0.04	0.18 ± 0.04	0.25 ± 0.14	0.86 ± 0.14	0.81 ± 0.15
1994	+	0.36 ± 0.03	15.1 ± 0.4	0.57 ± 0.05	0.15 ± 0.03	0.24 ± 0.05	0.45 ± 0.09	1.20 ± 0.21	0.63 ± 0.12
1995	+	0.24 ± 0.03	14.1 ± 0.4	0.36 ± 0.04	0.23 ± 0.03	0.20 ± 0.04	0.60 ± 0.08	0.73 ± 0.16	0.77 ± 0.18
1996	+	0.16 ± 0.03	13.6 ± 0.9	0.40 ± 0.05	0.27 ± 0.04	0.10 ± 0.02	0.61 ± 0.08	0.37 ± 0.07	1.47 ± 0.28
1997	+	0.19 ± 0.02	13.1 ± 0.3	0.28 ± 0.03	0.26 ± 0.02	0.06 ± 0.03	0.65 ± 0.04	0.25 ± 0.05	1.84 ± 0.35
1998	+	0.32 ± 0.04	15.3 ± 0.5	0.46 ± 0.06	0.16 ± 0.05	0.13 ± 0.07	0.49 ± 0.15	0.62 ± 0.17	1.16 ± 0.33
1999	*	0.48 ± 0.02	16.4 ± 0.2	0.63 ± 0.03	0.07 ± 0.03	0.15 ± 0.04	*	0.78 ± 0.15	1.27 ± 0.25
2000	*	0.44 ± 0.03	17.4 ± 0.3	0.72 ± 0.03	0.16 ± 0.03	0.21 ± 0.06	*	1.01 ± 0.22	1.11 ± 0.24
2001	−	0.45 ± 0.04	16.9 ± 0.4	0.65 ± 0.05	0.12 ± 0.04	0.19 ± 0.05	−0.33 ± 0.12	0.89 ± 0.22	1.18 ± 0.30
2002	−	0.47 ± 0.05	17.8 ± 0.4	0.77 ± 0.06	0.15 ± 0.04	0.21 ± 0.04	−0.57 ± 0.13	1.16 ± 0.18	1.02 ± 0.18
2003	−	0.45 ± 0.04	18.2 ± 0.3	0.92 ± 0.03	0.25 ± 0.05	0.23 ± 0.04	−0.88 ± 0.16	1.36 ± 0.16	0.92 ± 0.11
2004	−	0.46 ± 0.03	17.4 ± 0.3	0.74 ± 0.04	0.14 ± 0.03	0.29 ± 0.04	−0.41 ± 0.07	1.30 ± 0.16	0.85 ± 0.12
2005	−	0.48 ± 0.04	17.9 ± 0.3	0.83 ± 0.05	0.18 ± 0.03	0.19 ± 0.02	−0.51 ± 0.09	0.88 ± 0.10	1.35 ± 0.16
2006	−	0.36 ± 0.03	17.5 ± 0.4	0.64 ± 0.05	0.21 ± 0.03	0.22 ± 0.03	−0.45 ± 0.06	0.69 ± 0.10	1.44 ± 0.22
2007	−	0.33 ± 0.03	17.4 ± 0.2	0.65 ± 0.03	0.22 ± 0.02	0.15 ± 0.03	−0.43 ± 0.04	0.51 ± 0.06	1.87 ± 0.20
2008	−	0.27 ± 0.02	17.4 ± 0.3	0.64 ± 0.03	0.26 ± 0.02	0.17 ± 0.02	−0.49 ± 0.04	0.50 ± 0.07	1.85 ± 0.25
2009	−	0.21 ± 0.02	16.8 ± 0.3	0.45 ± 0.02	0.26 ± 0.02	0.12 ± 0.02	−0.44 ± 0.04	0.28 ± 0.04	2.76 ± 0.39
2010	−	0.34 ± 0.03	17.6 ± 0.3	0.62 ± 0.03	0.21 ± 0.04	0.18 ± 0.03	−0.43 ± 0.07	0.56 ± 0.08	1.72 ± 0.24
2011	−	0.35 ± 0.03	17.9 ± 0.3	0.67 ± 0.04	0.22 ± 0.03	0.26 ± 0.03	−0.53 ± 0.08	0.88 ± 0.10	1.17 ± 0.14
2012	*	0.36 ± 0.05	17.5 ± 0.3	0.62 ± 0.05	0.23 ± 0.04	0.26 ± 0.05	*	0.93 ± 0.17	1.12 ± 0.21
2013	*	0.38 ± 0.04	17.7 ± 0.3	0.65 ± 0.04	0.18 ± 0.04	0.24 ± 0.04	*	0.76 ± 0.14	1.34 ± 0.25

Notes. The amplitude and phase (the local solar time of maximum intensity) of the space harmonic vector in Figure 3, three components ($\xi_{\parallel}$, $\xi_{\perp}$, ξ_z) of the anisotropy in the solar wind frame in Figure 4 and modulation parameters ($G_{|z|}$, G_r, $\lambda_{\parallel}$) in Figure 5, all derived from the Nagoya MD data, are listed for each year. Yearly mean value and error are deduced from the average and dispersion of monthly values, respectively.

[a] Each character in the column "sgn(A)" indicates the polarity of the large-scale solar magnetic field assigned by us referring to the Solar Polar Field Strength available at the WSO Web site; "+" for a year in $A > 0$ epoch, "−" for a year in $A < 0$ epoch and "*" for a year when the polarity reversal is in progress (see the text).

(Levy 1976; Erdös & Kóta 1980; Potgieter & Moraal 1985). The reproduction of the NS anisotropy, which is formed by the interplay of drift and perpendicular diffusion, is more challenging for theoretical models. This is particularly true for the $A > 0$ epoch, when latitudinal gradients tend to point away from the current sheet, but the intensity minimum of GCRs is not precisely on the HCS. Hence, one cannot expect a one-to-one correlation between the field polarity and the NS anisotropy (Okazaki et al. 2008). Kóta & Jokipii (2001) modeled the 3D anisotropy in a simulation including a wavy HCS with possible variations in the solar wind speed leading to the formation of corotating interaction regions. Their results are in qualitative agreement with the observed phase shift and reduction of the radial gradient in the $A > 0$ epochs, as well as with oppositely directed (poleward vs. equatorward) latitudinal gradients in the $A > 0$ and $A < 0$ epochs, respectively. The simulation results for the variation in the NS anisotropy remained inconclusive.

It is important to keep in mind that solar cycles are not identical and, as mentioned in the previous section, long-term changes do occur. A particularly interesting recent example is the long and unusual last solar cycle, when the GCR intensity at the Earth reached a record-high level (Mewaldt at al. 2010). The most plausible explanation is that the magnetic field was the

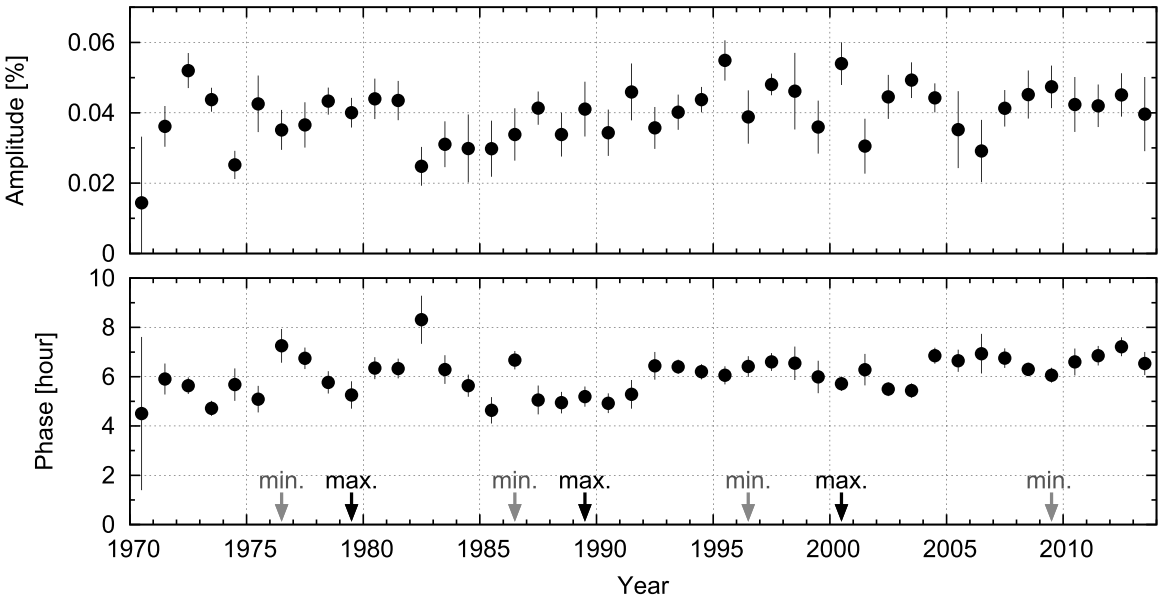

Figure 9. Long-term variation of the common vector. The yearly mean amplitude in % and the phase (denoted by the local solar time of the maximum intensity) in hours of the common vector are displayed in the upper and lower panels, respectively, each as a function of year on the horizontal axis. The common vector is introduced as a free parameter representing the atmospheric temperature effect on the diurnal anisotropy observed with the MD (see the text). The yearly mean and error are deduced from the means and dispersions of the monthly values, respectively. The solar maximum and minimum periods are indicated by black and gray arrows on the horizontal axis of the lower panel, respectively.

weakest ever recorded (McComas et al. 2008) and the weaker field allowed faster diffusion of GCRs into the inner part of the heliosphere. Another remarkable feature of the last solar cycle was that the HCS remained tilted for a long time and did not flatten the same way as in other cycles. Figure 4 shows that ξ_z turned out to be larger in the last solar minimum than during previous solar minima. This most likely shows the effect of the tilted HCS. The streaming component normal to the HCS cannot abruptly change, but has to change continuously at the HCS. Hence, ξ_z must be a small value when the HCS flattens, and it can be larger if the HCS is tilted. This feature is more apparent for the MD data than for the NM data.

The dynamic range of $\lambda_\parallel$ (or G_r) due to the 11 yr variation in the lower panels of Figure 7 is close to an order of magnitude and is much larger than the 22 yr variation. The small signature of its 22 yr variation can be easily masked by the 11 yr variation with a much larger amplitude. In order to analyze the 22 yr variation of each modulation parameter, therefore, it is necessary to minimize the influence of the 11 yr variation as much as possible. Simple means of $\lambda_\parallel$ and G_r in each of the $A > 0$ and $A < 0$ epochs may also be seriously biased by their long-term trends, as seen above. To identify the physical origin of the 22 yr variation correctly, it is also necessary to analyze its rigidity dependence. The long-term observation with the Nagoya MD, as well as the observations with NMs, makes such analyses possible.

This work is supported in part by the joint research programs of the Solar-Terrestrial Environment Laboratory (STEL), Nagoya University and the Institute of Cosmic Ray Research, University of Tokyo. The observations with the Nagoya multi-directional muon detector are supported by the Nagoya University. The Bartol Research Institute neutron monitor program, which operates Newark, Thule, and McMurdo neutron monitors, is supported by National Science Foundation grant ATM-0000315. We thank the World Data Center for Cosmic Rays, Solar-Terrestrial Environment Laboratory, Nagoya University, for providing the neutron monitor data analyzed in this paper. Wilcox Solar Observatory data used in this study was obtained via the Web site http://wso.stanford.edu at 2014:03:19_01:10:41 PDT courtesy of J. T. Hoeksema. The Wilcox Solar Observatory is currently supported by NASA. J. K. thanks STEL and Shinshu University for their support and hospitality during his stay as the visiting professor of STEL.

APPENDIX A

NUMERICAL DATA OF ANISOTROPY COMPONENTS AND MODULATION PARAMETERS OBTAINED IN THIS PAPER

For reference, we list in Table 2 numerical data of the anisotropy and modulation parameters derived from the MD data at 60 GV. Note that the amplitude and phase in these tables are corrected for the CG effect arising from the Earth's orbital motion around the Sun (see Section 2.2 in the text). We confirmed that the anisotropy components derived from NMs by us each year are fairly consistent with the components given in Paper I (see Table 2 in their paper), which analyzed the same NM data in a similar manner during an overlap period between 1970 and 1988. The amplitude and phase of the common vector derived in our analyses of the MD data are shown in Figure 9 (see the text). It is seen that the amplitude of the common vector is small and the phase is almost stable around ~06:00 local solar time.

APPENDIX B

DEPENDENCE ON THE UPPER LIMIT RIGIDITY

Following the analyses in Papers I and II, we assumed in this paper the rigidity spectrum of the anisotropy in Equation (9) with γ and P_u fixed at 0 and 100 GV respectively. This choice of the spectrum is rather subjective, lacking firm physical or observational proof. In this section, we show how β (the ratio between anisotropies and modulation parameters derived from

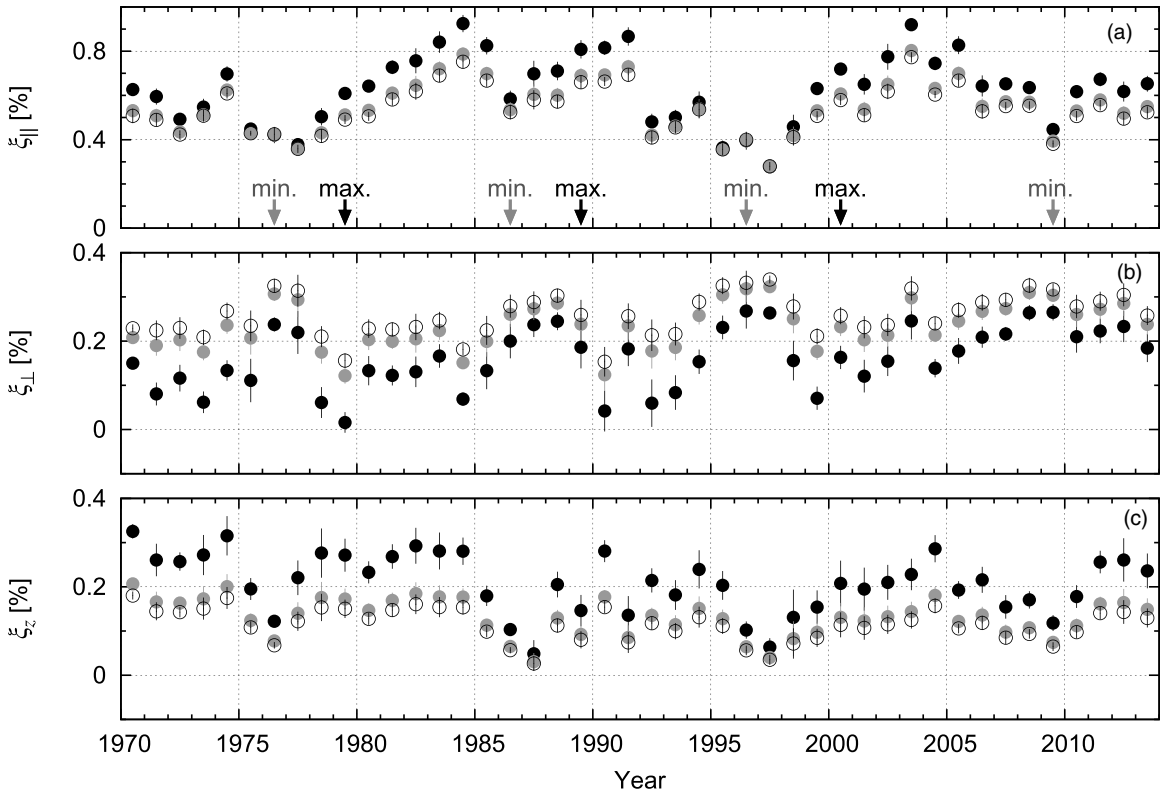

Figure 10. Three components of the free-space anisotropy derived from the MD data assuming P_u = 100, 200, 300 GV. Solid black, solid gray, and open circles represent the components obtained with P_u = 100, 200, 300 GV, respectively. The solar maximum and minimum periods are indicated by black and gray arrows on the horizontal axis of the top panel, respectively.

Table 3
Mean β Values Obtained with Three Different P_us in Equation (9)

	Polarity	$P_u = 100$ GV	$P_u = 200$ GV	$P_u = 300$ GV
$\beta_{\xi_\parallel}$	$A > 0$	0.77 ± 0.07	0.74 ± 0.06	0.75 ± 0.06
	$A < 0$	0.94 ± 0.05	0.84 ± 0.04	0.82 ± 0.04
	Mean	0.89 ± 0.05	0.81 ± 0.04	0.79 ± 0.04
$\beta_{\xi_\perp}$	$A > 0$	1.65 ± 0.35	2.24 ± 0.34	2.36 ± 0.33
	$A < 0$	1.26 ± 0.14	1.59 ± 0.14	1.70 ± 0.14
	Mean	1.35 ± 0.14	1.80 ± 0.13	1.93 ± 0.13
β_{ξ_z}	$A > 0$	4.45 ± 0.61	2.81 ± 0.39	2.45 ± 0.34
	$A < 0$	6.08 ± 0.96	3.82 ± 0.61	3.32 ± 0.53
	Mean	5.22 ± 0.55	3.29 ± 0.35	2.86 ± 0.31
$\beta_{G_{\lvert z\rvert}}$	$A > 0$	0.48 ± 0.10	0.68 ± 0.09	0.72 ± 0.09
	$A < 0$	0.35 ± 0.05	0.46 ± 0.05	0.49 ± 0.06
	Mean	0.39 ± 0.05	0.53 ± 0.05	0.57 ± 0.05
β_{G_r}	$A > 0$	0.85 ± 0.12	0.56 ± 0.08	0.50 ± 0.07
	$A < 0$	0.87 ± 0.13	0.58 ± 0.09	0.52 ± 0.08
	Mean	0.86 ± 0.08	0.57 ± 0.05	0.51 ± 0.05
$\beta_{\lambda_\parallel}$	$A > 0$	1.00 ± 0.13	1.44 ± 0.18	1.62 ± 0.20
	$A < 0$	1.16 ± 0.15	1.53 ± 0.19	1.65 ± 0.21
	Mean	1.08 ± 0.09	1.47 ± 0.12	1.61 ± 0.13

Notes. The β value is the ratio of the parameter derived from MD data at 60 GV to that derived from NM data at 17 GV (see text). Mean β values in $A > 0$ and $A < 0$ epochs and in the total period consisting of all $A > 0$ and $A < 0$ epochs are listed. Mean value and error are deduced from the average and dispersion of yearly values.

the NM and MD data) depends on the upper limiting rigidity (P_u) assumed and that our major conclusions on the rigidity dependence derived from β are not affected by changing P_u. Figure 10 displays anisotropy components derived from the MD data with three different P_u values. We choose a range of P_u between 100 and 300 GV based on the solar cycle variation of P_u reported in Munakata et al. (1997). We confirmed that the anisotropy derived from the NM data is almost insensitive to changing P_u as pointed out by Paper II, while the anisotropy derived from the MD data changes significantly. The increase in P_u with the same spectral index (γ) results in the reduction of the amplitude of the free-space anisotropy. It also results in the phase of the diurnal anisotropy in free space shifting to earlier hours, due to the reduced average deflection of GCR orbits in the geomagnetic field. Features of anisotropy components in Figure 10 changing with P_u are interpreted in terms of the nature of the free-space anisotropy. Table 3 lists the mean β for three P_u values. First, the mean $\beta_{\xi_\parallel}$ close to (or slightly smaller than) one for all P_u indicates $\xi_\parallel$ as being similar in the NM and MD data, while it is significantly smaller in $A > 0$ than in $A < 0$ for each P_u. Second, the mean $\beta_{\xi_\perp}$ and β_{ξ_z} are both significantly larger than one, indicating harder rigidity spectra of $\xi_\perp$ and ξ_z than that of $\xi_\parallel$. The mean β_{ξ_z} is always larger than the mean $\beta_{\xi_\perp}$. Third, the mean $\beta_{G_{|z|}}$ and β_{G_r} are significantly smaller than one for all P_u values.

REFERENCES

Agrawal, S. P. 1983, SSRv, 34, 127
Ahluwalia, H. S. 1988, GeoRL, 15, 287
Amenomori, M., Ayabe, S., Cui, S. W., et al. 2004, PhRvL, 93, 061101
Bieber, J. W., & Chen, J. 1991, ApJ, 372, 301 (Paper II)
Bieber, J. W., Evenson, P., & Matthaeus, W. 1987, GeoRL, 14, 864
Bieber, J. W., & Pomerantz, M. A. 1983, GeoRL, 10, 920
Bieber, J. W., & Pomerantz, M. A. 1986, ApJ, 303, 843
Cane, H. V., Richardson, I. G., & von Rosenvinge, T. T. 1996, JGR, 101, 21561

Chapman, S., & Bartels, J. 1940, Geomagnetism, Vol. 2 (Oxford: Oxford Univ. Press), 611
Chen, J., & Bieber, J. W. 1993, ApJ, 405, 375 (Paper I)
Compton, A. H., & Getting, I. A. 1935, PhRv, 47, 817
Cutler, D. J., & Groom, D. E. 1986, Natur, 322, 434
Erdös, G., & Kóta, J. 1980, Ap&SS, 67, 45
Forbush, S. E. 1967, JGR, 72, 4937
Fujimoto, K., Inoue, A., Murakami, K., & Nagashima, K. 1984, Coupling Coefficients of Cosmic Ray Daily Variations for Neutron Monitor Stations (CRRL Rep., No. 9; Nagoya: Cosmic-Ray Research Laboratory)
Gleeson, L. J. 1969, P&SS, 17, 31
Gleeson, L. J., & Axford, W. I. 1967, ApJL, 149, L115
Hall, D. L., Duldig, M. L., & Humble, J. E. 1996, SSRv, 78, 449
Hall, D. L., Duldig, M. L., & Humble, J. E. 1997, ApJ, 482, 1038
Hall, D. L., Humble, J. E., & Duldig, M. L. 1994, JGR, 99, 21433
Jokipii, J. R., & Kopriva, D. A. 1979, ApJ, 234, 384
Jokipii, J. R., & Kóta, J. 1982, GeoRL, 9, 656
Jordan, A. P., Spence, H. E., Blake, J. B., & Shaul, D. N. A. 2011, JGR, 116, A11103
King, J. H., & Papitashvili, N. E. 2005, JGR, 110, A02104
Kóta, J., & Jokipii, J. R. 1983, ApJ, 265, 573
Kóta, J., & Jokipii, J. R. 2001, AdSpR, 27, 607
Laurenza, M., Storini, M., Moreno, G., & Fujii, Z. 2003, JGR, 108, 1069
Levy, E. H. 1976, JGR, 81, 2082
Lin, Z., Bieber, J. W., & Evenson, P. 1995, JGR, 100, 23543
McComas, D. J., Ebert, R. W., Elliott, H. A., et al. 2008, GeoRL, 35, L18103
Mewaldt, R. A., Davis, A. J., Lave, K. A., et al. 2010, ApJL, 723, L1
Minnie, J., Bieber, J. W., Matthaeus, W. H., & Burger, R. A. 2007, ApJ, 670, 1149
Mori, S., & Nagashima, K. 1979, P&SS, 27, 39
Mori, S., Sagisaka, S., & Yasue, S. 1998, JGG, 40, 1023
Munakata, K., Miyasaka, H., Hall, D. L., et al. 1997, in Proc. 25th Int. Cosmic Ray Conf. (Durban), Vol. 2, Long-term Variation of Cosmic-ray Diurnal Anisotropy Observed by a Network of Multi-directional Muon Telescopes in a Wide Range of Rigidity, ed. M. S. Potgieter, B. C. Raubenheimer, & D. J. van der Walt (Transvaal: Potchefstroom University), 77
Munakata, K., Miyasaka, M., Sakurai, I., et al. 2002, AdSpR, 29, 1527
Murakami, K., Nagashima, K., Sagisaka, S., Mishima, Y., & Inoue, A. 1979, NCimC, 2C, 635
Nagashima, K., Fujimoto, K., Fujii, Z., Ueno, H., & Kondo, I. 1972, Rep. Ionos. Space Res. Jpn., 26, 31
Oh, S. Y., Yi, Y., & Bieber, J. W. 2010, SoPh, 262, 199
Okazaki, Y., Fushishita, A., Narumi, T., et al. 2008, ApJ, 681, 693
Palmer, I. D. 1982, RvGSP, 20, 335
Parker, E. N. 1958, ApJ, 128, 664
Parker, E. N. 1965, P&SS, 13, 9
Potgieter, M. S., & Moraal, H. 1985, ApJ, 294, 425
Swinson, D. B. 1969, JGR, 74, 5591
Thambyahpillai, T., & Elliot, H. 1953, Natur, 171, 918
Yasue, S. 1980, JGG, 32, 617
Yasue, S., Sakakibara, S., & Nagashima, K. 1982, Coupling Coefficients of Cosmic Ray Daily Variations for Neutron Monitor Stations (CRRL Rep., No. 7; Nagoya: Cosmic-Ray Research Laboratory)